Two-dimensional Peierls instability via zone-boundary Dirac line nodes in layered perovskite oxides

Jin-Hong Park,[1] Seung Hun Lee,[1,2] Choong H. Kim,[1,2] Hosub Jin,[3,*] and Bohm-Jung Yang[1,2,4,†]

[1]*Center for Correlated Electron Systems, Institute for Basic Science (IBS), Seoul 08826, Korea*
[2]*Department of Physics and Astronomy, Seoul National University, Seoul 08826, Korea*
[3]*Department of Physics, Ulsan National Institute of Science and Technology (UNIST), 50 UNIST, Ulsan 44919, South Korea*
[4]*Center for Theoretical Physics (CTP), Seoul National University, Seoul 08826, Korea*

Interplay of Fermi surface topology and electron correlation is the quintessential ingredient underlying spontaneous symmetry breaking in itinerant electronic systems. In one-dimensional (1D) systems at half filling, the inherent Fermi surface nesting makes the translationally invariant metallic state unstable, which is known as Peierls instability. Extending the scope of Peierls instability to two (2D) or three dimensions (3D), however, is not straightforward, since the Fermi surface in higher dimensions is generally not nested. In this work, we show that a perfectly nested Fermi surface can be realized in a class of 2D perovskite oxides, giving rise to 2D Peierls instability. Here the central role is played by the zone-boundary Dirac line node (DLN) protected by two orthogonal glide mirrors induced by the rotation of oxygen octahedra. Especially at a critical angle of the octahedron rotation, the zone-boundary DLN flattens, leading to logarithmically diverging susceptibility. We propose the 2D Peierls instability driven by dispersionless DLN as a principle mechanism for spontaneous symmetry breaking in various layered perovskite oxides including the antiferromagnetism of Sr_2IrO_4. As a clear signature of the 2D Peierls instability, we predict that the magnetic domain wall in Sr_2IrO_4 hosts localized soliton modes.

I. INTRODUCTION

Peierls instability is a ubiquitous mechanism originally suggested in a one-dimensional (1D) lattice at half filling that leads to the spontaneous dimerization [1]. Due to the inherent nesting of the 1D Fermi surface topology, the translationally invariant metallic state becomes unstable even in the presence of an infinitesimally weak interaction, manifested by the logarithmic divergence in its static susceptibility at the momentum $q = 2k_F$ where k_F indicates the Fermi momentum [Fig. 1(a)]. In two (2D) or three dimensions (3D), however, the Fermi surface nesting is less likely, and the metallic state is stable as long as there is no effective attraction between electrons on the Fermi surface and the repulsive interaction between them is smaller than a certain threshold value [2]. Thus the interplay of Fermi surface topology and electron correlation lies at the heart of the weak coupling instability of the metallic state with translational invariance.

As an attempt to realize a 2D Peierls system, the laterally stacked 1D Peierls system can be constructed. For a 1D Peierls building block, let us consider a well-known polyacetylene chain at its critical point preserving the translation symmetry. In this system, Fermi surface nesting occurs in the form of a 1D Dirac point at the Brillouin zone (BZ) boundary [Fig. 1(b)]. By considering 1D polyacetylene chains at the critical point as being embedded in 2D, the 1D Dirac point can be extended to a flat Dirac line node (DLN) spanning the 2D BZ boundary. Therefore, the 2D extension of the

Peierls instability is clued by the presence of dispersionless zone-boundary DLN at the critical point. In general, however, it is not easy to protect a line degeneracy in 2D systems, especially when both time-reversal T and inversion P symmetries exist together with spin-orbit coupling. In fact, even the zone-boundary 1D Dirac point in a polyacetylene chain at its critical point is not a symmetry protected degeneracy but merely resulting from the unit cell doubling.

All those difficulties are remediable in the presence of nonsymmorphic crystalline symmetries such as glide mirrors or screw rotations, which is known to protect band degeneracies at the BZ boundary in general [3]. For instance, let us deform a straight 1D chain at its critical point to a zigzag form as shown in Fig. 1(c). Due to the unit cell doubling, the deformed chain has a 1D Dirac point at the BZ boundary. Moreover, the deformation makes the zigzag chain invariant under a mirror or a twofold rotation symmetry combined with a half translation along the chain direction, that is, a glide mirror or a twofold screw rotation symmetry is induced by the lattice deformation. Such an induced nonsymmorphic symmetry renders the zone-boundary Dirac point symmetry protected, thus it remains gapless as long as the corresponding nonsymmorphic symmetry is preserved [Fig. 1(d)] [4]. Arbitrary stacking of the zigzag-shaped chain does not guarantee a line degeneracy along the BZ boundary, since the combination of the twofold screw rotation and inversion can at most protect the fourfold degeneracy only at a point [Fig. 1(e)] [5]. However, when the stacked chain system preserves the glide mirror of a 1D chain and has an additional in-plane mirror symmetry embracing the 2D plane, the fourfold degeneracy of the zone-boundary DLN can remain intact even in the presence of spin-orbit coupling [Fig. 1(f)]. Moreover, if the bandwidth of the symmetry-protected zone-boundary DLN

*Corresponding author: hsjin@unist.ac.kr
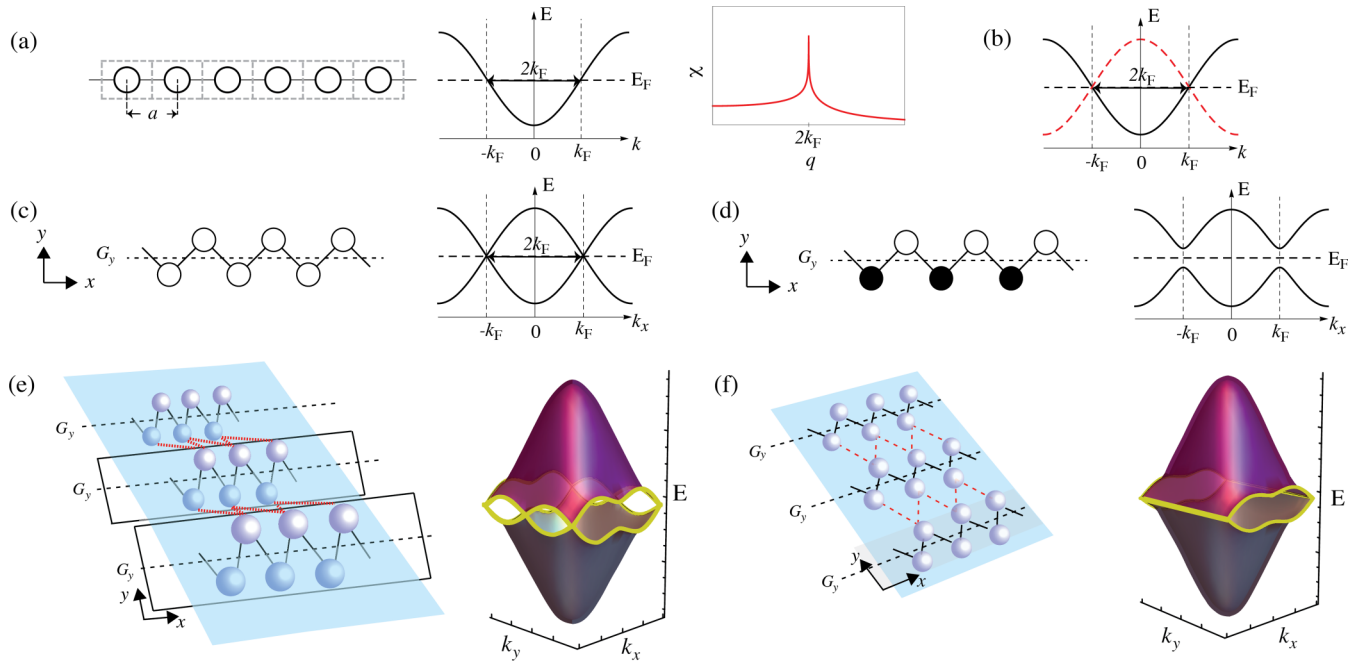†Corresponding author: bjyang@snu.ac.kr

FIG. 1. Peierls instability and glide mirror in one dimension (1D) and two dimensions (2D). (a) A monatomic chain having a single electron per site has a nested half-filled band structure with the Fermi momentum k_F. The relevant static susceptibility $\chi(q)$, which diverges logarithmically at the wave vector $q = 2k_F$. (b) Band structure at the critical point after zone folding. (c) A zigzag shaped 1D chain having induced glide mirror symmetry and the resulting band structure. Here the band degeneracy at the BZ boundary at $k = \pm k_F$ is protected by the glide mirror induced by the lattice deformation. (d) Consequence of glide symmetry breaking. Here the white and black dots indicate the two sites with different on-site potentials resulting from electron correlation. (e) A 2D system composed of coupled 1D chains. A generic structure with a twofold screw rotation can protect only a few Dirac points at the Brillouin zone (BZ) boundary. (f) When the coupled 1D chains have an additional mirror symmetry about the 2D plane together with the original glide mirror, a Dirac line node appears along a BZ boundary.

can be controlled to become completely dispersionless, 2D Peierls instability can occur, leading to various symmetry breaking phenomena.

Here we show that such an intriguing idea can be realized in a wide class of layered perovskite oxides. The central role is played by the in-plane rotation of oxygen octahedra, which is a common lattice distortion among layered 2D perovskite oxides. It doubles the size of the unit cell and, at the same time, generates two orthogonal glide mirrors, leading to the DLN at the BZ boundary. Interestingly, the bandwidth of the nodal line dispersion can be controlled by changing the in-plane rotation angle θ of oxygen octahedra. When θ reaches a certain critical value θ_c, the DLN on the BZ boundary becomes completely dispersionless, manifesting 2D Peierls instability with the logarithmically diverging susceptibility. We propose that the instability induced by the dispersionless zone-boundary DLN is the principle mechanism for the canted antiferromagnetic ground state of Sr_2IrO_4. Given the magnetic ground state as a consequence of 2D Peierls instability, a magnetic domain wall (DW) of Sr_2IrO_4 is shown to host 1D localized soliton modes along the DW boundary. Since the origin of such a flat DLN is solely coming from the crystalline symmetry, we believe that the 2D Peierls instability can occur ubiquitously in various layered perovskite oxides sharing the same crystalline symmetry.

The outline of this paper is as follows. The rotation distortion induced nonsymmorphic crystalline symmetries are described in Sec. II. In Sec. III, we present the nonsymmor-

phic symmetry protection of the DLN on the BZ boundary. The bandwidth of the DLN can be controlled by rotation angle of octahedra, which is discussed in Sec. IV. In Sec. V we explain the mechanism of the dispersionless DLN by the localized line states. The magnetic instability induced by the dispersionless DLN on the BZ boundary is discussed in Sec. VI. As a consequence of 2D Peierls instability, we predict the domain wall fermion in Sec. VII, which is followed by the discussion in Sec. VIII. The detailed analysis about the DLN with fourfold degeneracy along the BZ boundary can be found in Appendix A. The details of the hopping parameters of the tight-binding Hamiltonian is given in Appendix B. The controllable bandwidth is supported by the DFT calculations in Appendix C. The stability of DLN including staggered tetragonal distortion is presented in Appendix D. We perform susceptibility calculations in the presence of sublattice, spin, and layer degrees of freedom in Appendix E. In Appendix F, the detailed information about the self-consistent mean-field calculation is provided. We explain the dispersionless DLN by the diagonal localized line states in Appendix G. Finally, the detailed analysis on the magnetic domain wall fermion is given in Appendix H.

II. LATTICE DISTORTION INDUCED NONSYMMORPHIC SYMMETRY

Layered perovskite oxides with the chemical formula A_2BO_4, as shown in Fig. 2(a), normally undergo several
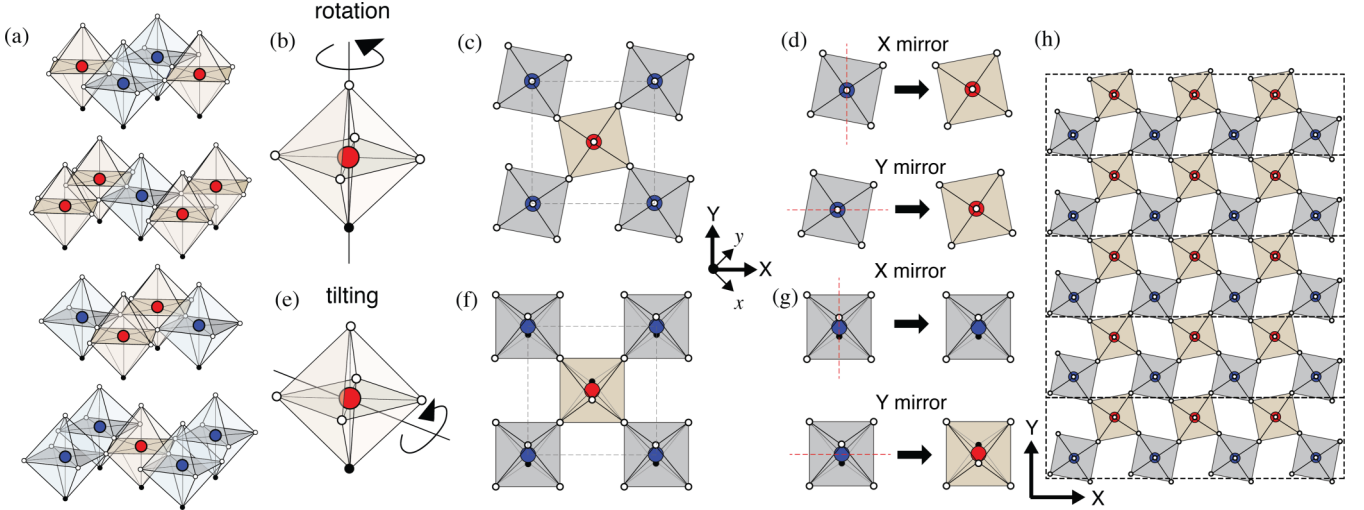
FIG. 2. Rotation of oxygen octahedra and induced glide mirror in layered perovskite oxides. (a) Three-dimensional (3D) structure of a layered perovskite oxide. (b) Rotation distortion of an octahedron due to the rotation about the Z axis. (c) Structure of a layer with the rotation distortion. (d) Operation of the mirror symmetry about the YZ plane (X mirror) and XZ plane (Y mirror) on a layer with rotation distortion. (e) Tilting distortion of an octahedron due to the rotation about an in-plane axis. (f) Structure of a layer with the tilting distortion. (g) Operation of the mirror symmetry about YZ and XZ planes on a layer with the tilting distortion. (h) A two-dimensional (2D) layer with rotation distortion can be considered as a coupled one-dimensional (1D) zigzag chain with G_Y symmetry stacked along the Y direction.

kinds of structural distortions [6]. The most widely occurring distortions are the in-plane rotation of oxygen octahedra about the z axis [rotation distortion, see Fig. 2(b)] and another rotation of oxygen octahedra about an axis lying in the 2D plane [tilting distortion, see Fig. 2(e)]. Both rotation and tilting distortions double the size of the in-plane unit cell as shown in Figs. 2(c) and 2(f), and the relative orientation of the distorted octahedra between layers determines the overall space group symmetry of the 3D structure. In many cases, the bulk properties are mainly determined by the property of a monolayer due to the weak interlayer coupling.

There are several materials exhibiting rotation distortion [7–11]. For instance, Sr_2IrO_4 undergoes a rotation distortion of oxygen octahedra with the angle $\theta \sim 11°$ in a staggered manner leading to the $\sqrt{2} \times \sqrt{2}$-type doubled unit cell before the antiferromagnetic (AFM) ordering is developed [7]. [See Fig. 2(c).] A similar distortion is observed in Refs. [8,9] with $\theta \sim 9°$. Such an in-plane rotation distortion changes the space group symmetry of the lattice from the symmorphic group $I4/mmm$ (no. 139) to the nonsymmorphic group $I4_1/acd$ (no. 142) [10] exhibiting two orthogonal glide mirrors [Fig. 2(d)]. Below we show that the nonsymmorphic symmetry induced by the rotation brings about remarkable physical consequences.

Explicitly, the two glide mirrors $G_{X,Y} \equiv \{M_{X,Y}|\frac{1}{2}\frac{1}{2}\}$ are the combination of an ordinary mirror $M_{X,Y}$ which inverts the sign of the X or Y coordinate and a partial translation $(\frac{1}{2}, \frac{1}{2})$ along the diagonal direction [see Fig. 2(d)]. Here we choose the $\sqrt{2} \times \sqrt{2}$-type doubled cell as a unit cell, and then the translations of the unit cell along the X and Y directions span the whole 2D lattice as shown in Fig. 2(h). The whole lattice can be viewed as a vertical stacking of horizontal zigzag chains analogous to Fig. 1(f). The presence of these two orthogonal glide mirrors together with time-reversal T and inversion P guarantees the presence of a Dirac line node

with fourfold degeneracy along the BZ boundary as explained in detail below.

Let us note that, in the case of the tilting distortion [12], which exists in various materials including La_2CuO_4 and T-phase cuprates [13,14], the distorted lattice hosts only one glide mirror as shown in Fig. 2(g), which can protect at most Dirac point nodes on the BZ boundary as shown in Ref. [15]. In this case, one cannot expect a significant enhancement of the susceptibility, thus we neglect the tilting distortion and focus on the rotation distortion in the forthcoming discussion.

III. DIRAC LINE NODES (DLN) ON THE BRILLOUIN ZONE BOUNDARY

The two glide mirrors induced by the rotation distortion of oxygen octahedra can generate the fourfold degenerate DLN on the full BZ boundary due to the following reason. The point group symmetry of the system is generated by inversion P, and two glide mirrors G_X and G_Y, which transform the spatial coordinate as

$$P : (X, Y) \rightarrow (-X, -Y),$$
$$G_X : (X, Y) \rightarrow \left(-X + \tfrac{1}{2}, Y + \tfrac{1}{2}\right) \times i\sigma_X, \qquad (1)$$
$$G_Y : (X, Y) \rightarrow \left(X + \tfrac{1}{2}, -Y + \tfrac{1}{2}\right) \times i\sigma_Y,$$

where $\sigma_{X,Y,Z}$ indicate the spin Pauli matrices. By combining P and $G_{X,Y}$, one can also define two twofold screw rotations $S_X \equiv G_X P$ and $S_Y \equiv G_Y P$ and an in-plane mirror $M_Z \equiv G_X G_Y P$. In general, when P and T exist simultaneously, every band is doubly degenerate at each momentum. Due to the strong level repulsion between degenerate bands, it is not easy to achieve band crossing without proper additional symmetries [15], which in the present case are G_X and G_Y.

Explicitly, let us first explain the role of G_Y in protecting the band degeneracy along the BZ boundary, $k_X = \pm\pi$. As

shown in Fig. 2(h), the distorted 2D lattice with rotation distortion can be considered as coupled 1D chains having G_Y. Since each chain hosts Dirac points at the BZ boundary with $k_X = \pm\pi$, the distorted 2D lattice can have a DLN along the BZ boundary with $\mathbf{k} = (\pm\pi, k_Y)$ [$k_Y \in (-\pi, \pi)$]. On the BZ boundary, the system is invariant under PT, $M_Z = G_X G_Y P$, and $S_Y = G_Y P = \{C_{2Y}|(\frac{1}{2}, \frac{1}{2})\}$ where $C_{2Y} \equiv M_Y P$ is an ordinary twofold rotation about the Y axis. Let us note that S_Y contains a half translation along the X direction perpendicular to its rotation axis. This indicates that the rotation axis of S_Y is not located at the inversion center, that is, S_Y is an off-centered twofold rotation symmetry [16]. Because of such an off-centered nature of S_Y, it anticommutes with PT on the BZ boundary

$$PT S_Y = -e^{-ik_Y} S_Y PT, \tag{2}$$

which forces each Kramers pair on the BZ boundary to carry the same S_Y eigenvalues, i.e., either $+ie^{ik_Y/2}$ or $-ie^{ik_Y/2}$ (see Appendix A and Ref. [16]). Then a DLN with fourfold degeneracy can occur, if two different Kramers pairs having distinct S_Y eigenvalues are degenerate due to the presence of an additional symmetry. In fact, this is exactly the role played by M_Z symmetry. Let us note that the spin orientation of S_Y (M_Z) eigenstates is parallel to the Y (Z) axis since $S_Y \propto i\sigma_Y$ ($M_Z \propto i\sigma_Z$) due to spin-orbit coupling. The orthogonal spin orientation between S_Y and M_Z eigenstates indicates the following anticommutation relation

$$M_Z S_Y = -S_Y M_Z, \tag{3}$$

which, combined with Eq. (2), guarantees the fourfold degeneracy of the relevant DLN. The DLN on the BZ boundary $k_Y = \pm\pi$ can also be understood in a similar way. Therefore, the DLN spanning the full BZ boundary arises from the presence of two orthogonal glide mirrors in systems with P and T symmetries.

IV. TUNING THE BANDWIDTH OF THE DLN VIA ROTATION DISTORTION

To demonstrate the presence of the DLN spanning the BZ boundary and how to control its bandwidth, we study a tight-binding Hamiltonian relevant to Sr_2IrO_4. Sr_2IrO_4 is a representative system in which the interplay of strong spin-orbit coupling and electron correlation can give rise to novel spin-orbit entangled ground states [17–22]. Since strong spin-orbit coupling splits $5d$ t_{2g} orbitals into a lower energy quartet and a higher energy doublet with the effective angular momentum $J_{\text{eff}} = 3/2$ and $J_{\text{eff}} = 1/2$, respectively, an Ir^{4+} ion has a half-filled $J_{\text{eff}} = 1/2$ state and fully-occupied $J_{\text{eff}} = 3/2$ states. Thus, the low energy band structure near the Fermi energy is dominated by the Ir $J_{\text{eff}} = 1/2$ states, from which a lattice model Hamiltonian can be constructed.

The unit cell of Sr_2IrO_4 is composed of four layers of iridium oxide planes. For convenience, however, we first focus on the property of a single iridium oxide layer and then include the influence of weak interlayer coupling. By introducing $\psi^\dagger(\mathbf{k}) = [c_{A,\uparrow}^\dagger(\mathbf{k}), c_{A,\downarrow}^\dagger(\mathbf{k}), c_{B,\uparrow}^\dagger(\mathbf{k}), c_{B,\downarrow}^\dagger(\mathbf{k})]$ as a basis, the lattice Hamiltonian for a single layer with a rotation distortion of an oxygen octahedron by an angle θ [see Fig. 3(a)] can be written as $\hat{H}_\theta = \sum_{\mathbf{k}} \psi^\dagger(\mathbf{k}) H(\mathbf{k}, \theta) \psi(\mathbf{k})$ in

which

$$\begin{aligned} H(\mathbf{k}, \theta) = {} &\varepsilon_1(\mathbf{k}, \theta)\sigma_0\tau_x + \varepsilon_{1d}(\mathbf{k}, \theta)\sigma_z\tau_y \\ &+ [\varepsilon_2(\mathbf{k}, \theta) + \varepsilon_3(\mathbf{k}, \theta)]\sigma_0\tau_0, \end{aligned} \tag{4}$$

where $\varepsilon_{1,1d}(\mathbf{k}, \theta) = 2t_{1,1d}(\theta)[\cos(k_x) + \cos(k_y)]$, $\varepsilon_2(\mathbf{k}, \theta) = 4t_2(\theta)\cos k_x \cos k_y$, $\varepsilon_3(\mathbf{k}, \theta) = 2t_3(\theta)[\cos(2k_x) + \cos(2k_y)]$. Here we choose the unit translation vectors $\hat{x}$ and $\hat{y}$ of the undistorted lattice as a unit of real space coordinates for convenience. The explicit form of the hopping integral $t_{1,1d,2,3}(\theta)$ is shown in Appendix B. The Pauli matrices $\tau_{0,x,y,z}$ ($\sigma_{0,x,y,z}$) denote the A and B sublattice (the $J_{\text{eff}} = 1/2$ pseudospin) degrees of freedom. The diagonal term $\varepsilon_2(\mathbf{k}, \theta)$ [$\varepsilon_3(\mathbf{k}, \theta)$] indicates the second (third) nearest neighbor hopping processes between the same sublattices with the same effective angular momenta. The θ dependence of the hopping integrals is derived from the Slater-Koster approximation [23].

From Eq. (4), we have obtained the evolution of the band structures as a function of the rotation angle θ, which is shown in Figs. 3(b)–3(g). The presence of the DLN spanning the full BZ boundary is clearly observed. The band structure of Sr_2IrO_4 with its rotation angle $\theta \sim 11°$ matches well with the previously reported results [7]. It is worthwhile to note that the overall bandwidth of the DLN on the BZ boundary strongly depends on θ. Especially when $\theta \sim 16°$, the DLN becomes completely flat as depicted in Figs. 3(a) and 3(e). Then the resulting semimetal with zone-boundary DLN should be unstable even in the presence of an infinitesimally small interaction, which indeed links to the 2D Peierls instability.

The emergence of the flat DLN under rotation distortion is further supported by *ab initio* density functional theory (DFT) calculations including spin-orbit coupling as shown in Figs. 3(h)–3(q). To observe the θ dependence in DFT band structure, the in-plane lattice constant is varied while the Ir-O bond length is fixed. Figures 3(h)–3(l) show the evolution of DFT band structure for a single Sr_2IrO_4 layer. During the variation of the rotation angle θ, the bandwidth of the zone-boundary DLN (M-X line) also changes, consistent with the tight-binding calculations. The fourfold degenerate DLN eventually becomes almost flat around the critical angle $\theta \sim 23°$ as shown in Fig. 3(j). For the bulk Sr_2IrO_4 where the unit cell is composed of four monolayers, four distinct DLNs derived from $J_{\text{eff}} = 1/2$ states on the BZ boundary are displayed in Figs. 3(m)–3(q). Since G_X, G_Y, P, T symmetries are all preserved in the 3D structure, the fourfold degeneracy of each DLN is maintained. The nearly degenerate DLNs along the BZ boundary (M-X line) around the Fermi level become almost dispersionless at the critical angle $\theta \sim 23°$ as shown in Fig. 3(o). Although the critical angle predicted by the DFT calculations is not the same as that from the tight-binding calculations, the overall θ dependence of the zone-boundary DNL indicates the consistency between them. To provide additional evidence for the tunability of the DLN via rotation distortion, we also have examined another type of θ variation, which is obtained by changing the Ir-O bond length while the in-plane lattice constant is fixed. One can again observe the emergence of the flat bands at a certain critical angle θ in both a monolayer and the bulk system,
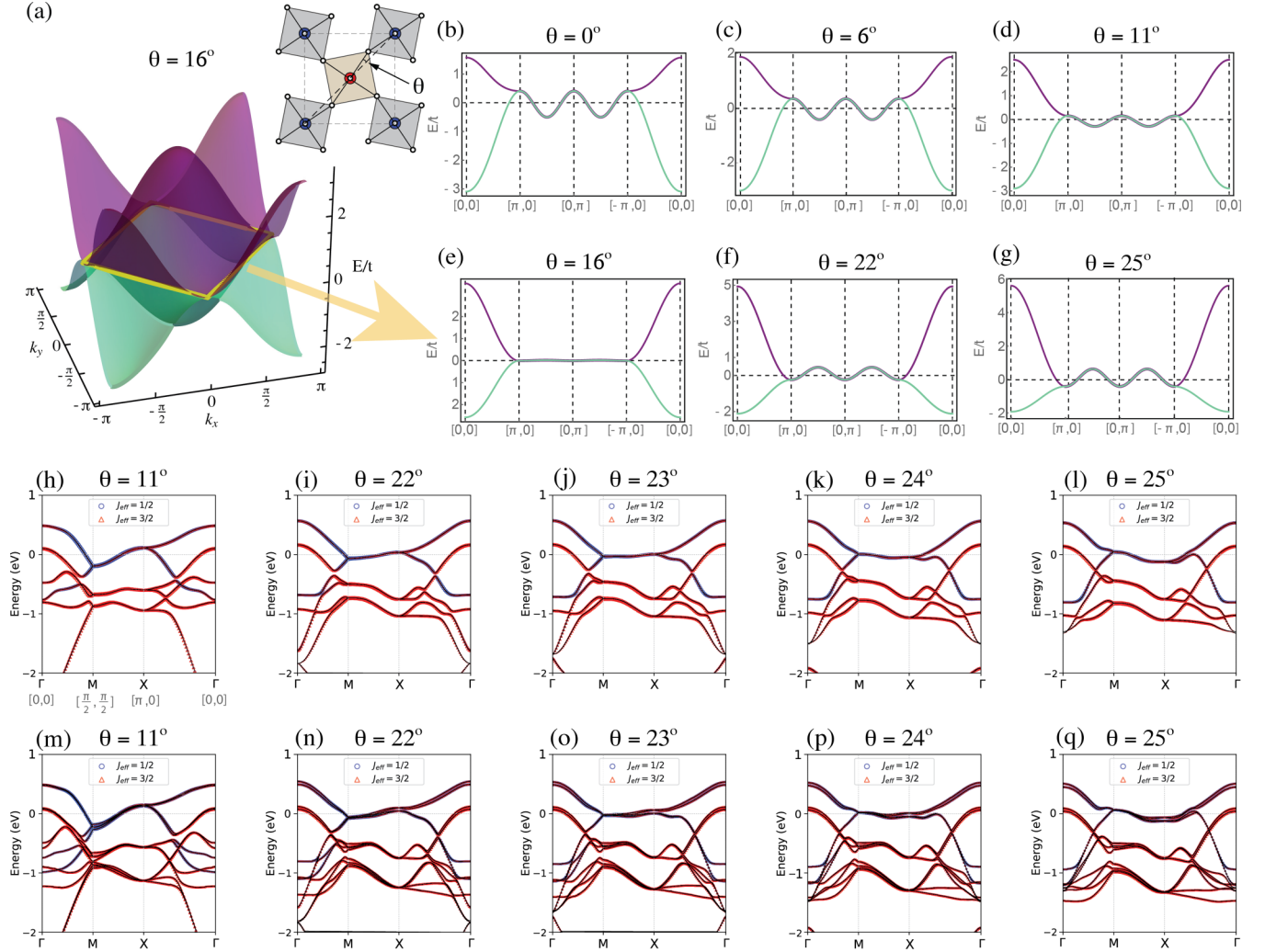
FIG. 3. Dispersion of the Dirac line node (DLN) as a function of in-plane rotation angle θ in Sr_2IrO_4. The band structures in (a)–(g) are from tight-binding calculations while those in (h)–(q) are from first-principles calculations. (a) The paramagnetic band structure of a single Sr_2IrO_4 layer when $\theta = 16°$. Here the DLN is dispersionless along the full Brillouin zone boundary. The definition of the rotation angle θ relative to the undistorted lattice structure is also described. (b)–(g) Dispersion of the DLN as θ varies. Here the purple and green lines are doubly degenerate. The DLN becomes completely flat at the critical angle $\theta \approx 16°$. (h)–(l) DFT band structures of a single Sr_2IrO_4 layer as θ varies while the Ir-O bond length is fixed. $J_{eff} = 1/2$ (blue circle) and $J_{eff} = 3/2$ (red triangle) bands are displayed by using different colors. The DLNs along the BZ boundary (M-X line) around the Fermi level become dispersionless at the critical angle $\theta \approx 23°$. (m)–(q) DFT band structures of the bulk Sr_2IrO_4 as θ varies while the Ir-O bond length is fixed. All symbols and colors are the same as in the case of a single Sr_2IrO_4 layer of (h)–(l). The DLNs along the BZ boundary (M-X line) around the Fermi level become almost dispersionless at the critical angle $\theta \approx 23°$.

which supports the robustness of our theory on the bandwidth-controllable DNL. (For details, see Appendix C 2.)

V. DISPERSIONLESS DLN AND THE LOCALIZED LINE STATES

When a band is completely dispersionless, it can be expressed as a linear combination of spatially localized eigenstates of the Hamiltonian. To fully account for the origin of the flat DLN on the BZ boundary, let us first consider a localized state shown in Fig. 4 defined along a diagonal line in the $2N \times 2N$ square lattice as

$$|\Psi\rangle_{\ell_\alpha,\sigma}^\alpha = \frac{1}{\sqrt{2N}} \sum_{\mathbf{r}\in\ell_\alpha} (-1)^{r_x} c_\sigma^\dagger(\mathbf{r})|0\rangle, \quad (5)$$

where $\ell_{\alpha=p,n} = 1, 2, ..., 2N$ is the labeling for a diagonal line with positive ($\alpha = p$) or negative ($\alpha = n$) slope, while a diagonal line with odd (even) ℓ_α is composed of sites belonging to the A(B) sublattice. $\mathbf{r} = (r_x, r_y)$ indicates the coordinate of a lattice site, and $\sigma = \pm$ denotes the effective angular momentum $J_{eff,z} = \pm 1/2$. Basically, $|\Psi\rangle_{\ell_\alpha,\sigma}^\alpha$ represents a line of states whose local wave function amplitude changes the sign alternatively along the line. Illustrations of such diagonal line states with positive and negative slopes are shown in Figs. 4(d) and 4(e).

A strictly localized wave function can be an eigenstate of the Hamiltonian only when the sum of hopping amplitudes onto sites outside the support of the wave function vanishes [24]. To examine the condition for $|\Psi\rangle_{\ell_\alpha,\sigma}^\alpha$ to be an eigenstate
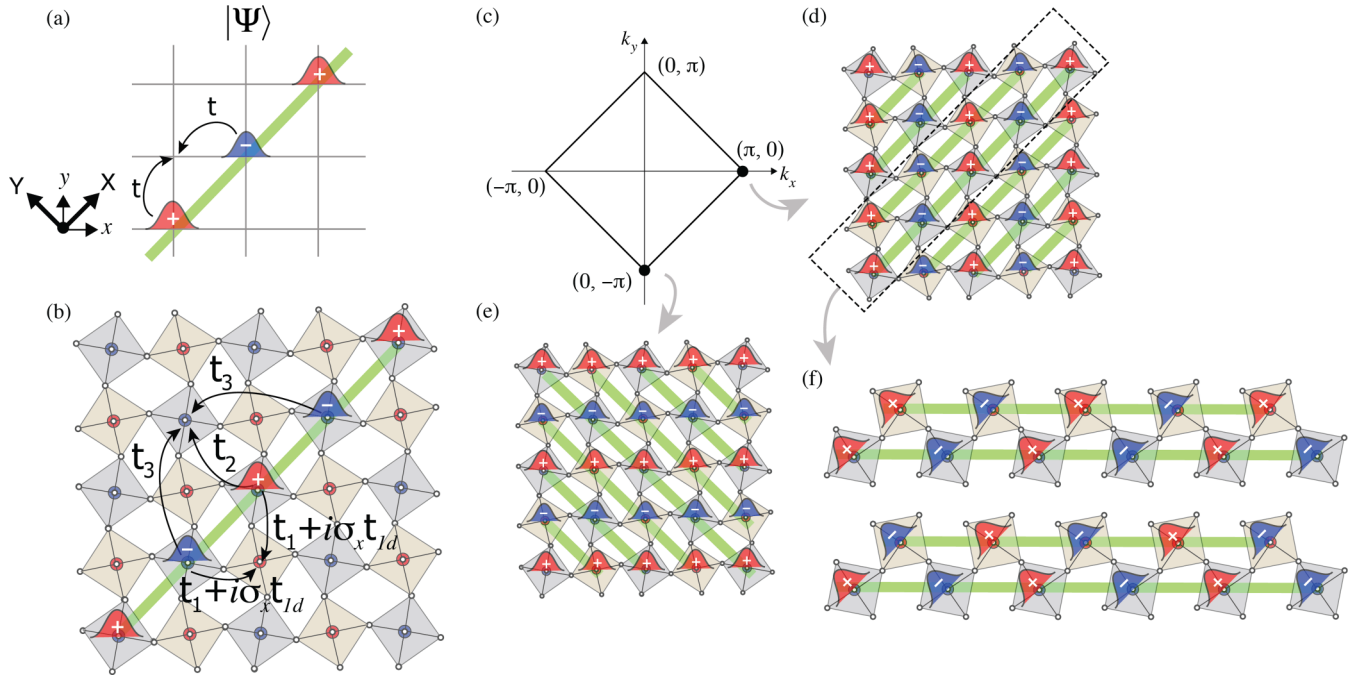
FIG. 4. The origin of the flat Dirac line node (DLN) and the relevant localized line states. (a) Illustration of the origin of a localized line state. The hopping amplitudes from two neighboring sites on a line to the common nearest neighbor site are canceled when the sign of the wave function alternates along the line. (b) The hopping processes from a localized line state to its first, second, and third nearest neighbor sites. (c)The first Brillouin zone. (d) The wave function of the flat DLN at the momentum $\boldsymbol{k} = (\pi, 0)$. (e) The wave function of the flat DLN at the momentum $\boldsymbol{k} = (0, -\pi)$. (f) Two neighboring localized line states can form two degenerate eigenstates of a zigzag shaped chain with the momentum π. Including spin degrees of freedom, the localized line states can span four degenerate states with the momentum π.

of the Hamiltonian, we first consider the hopping processes between nearest-neighbor sites described by the following Hamiltonian

$$\hat{H}_1 = t_1(\theta) \sum_{\langle \boldsymbol{r}, \boldsymbol{r}' \rangle, \sigma} \left[c_\sigma^\dagger(\boldsymbol{r}) c_\sigma(\boldsymbol{r}') + \text{H.c.} \right]$$
$$+ t_{1d}(\theta) \sum_{\langle \boldsymbol{r}, \boldsymbol{r}' \rangle, \sigma} \sigma \left[i c_\sigma^\dagger(\boldsymbol{r}) c_\sigma(\boldsymbol{r}') + \text{H.c.} \right], \quad (6)$$

where $\langle \boldsymbol{r}, \boldsymbol{r}' \rangle$ denotes a pair of nearest-neighbor sites belonging to different sublattices located at $\boldsymbol{r}$ and $\boldsymbol{r}'$, respectively. In momentum space, $\hat{H}_1$ gives rise to the terms $\varepsilon_{1/1d}(\mathbf{k}, \theta) = 2t_{1/1d}(\theta)[\cos(k_x) + \cos(k_y)]$ in Eq. (4). By applying $\hat{H}_1$ to $|\Psi\rangle_{\ell_\alpha, \sigma}^\alpha$, one can easily find that $\hat{H}_1 |\Psi\rangle_{\ell_\alpha, \sigma}^\alpha = 0$. Namely, due to the alternating sign of the wave function along the line, the hopping amplitudes to neighboring sites are canceled [see Fig. 4(a)], thus $|\Psi\rangle_{\ell_\alpha, \sigma}^\alpha$ becomes a localized eigenstate with zero energy. Therefore the diagonal line states $\{|\Psi\rangle_{\ell_\alpha, \sigma}^\alpha\}$ form a set of $8N$ independent and degenerate localized eigenstates.

Now we construct momentum eigenstates by taking a suitable linear combination of the localized diagonal line states as follows

$$|\Psi\rangle_{A, \sigma}^\alpha(\phi) = \frac{1}{\sqrt{N}} \sum_{m=1}^N e^{i2m\phi} |\Psi\rangle_{\ell_\alpha = 2m, \sigma}^\alpha,$$

$$|\Psi\rangle_{B, \sigma}^\alpha(\phi) = \frac{1}{\sqrt{N}} \sum_{m=1}^N e^{i(2m-1)\phi} |\Psi\rangle_{\ell_\alpha = (2m-1), \sigma}^\alpha. \quad (7)$$

As shown in Appendix G, it is straightforward that $|\Psi\rangle_{A, \sigma}^p(\phi)$ is a plane wave state with momentum $\boldsymbol{k}$ satisfying $k_x + k_y = \pi$. Likewise, one can check that $|\Psi\rangle_{B, \sigma}^p(\phi)$ is another plane wave state with the same momentum. Taking the pseudospin σ into account, we have found four linearly independent degenerate eigenstates which are dispersionless along the BZ boundary satisfying $k_x + k_y = \pi$. By repeating similar procedures, one can also show that $\{|\Psi\rangle_{A/B, \sigma}^n(\phi)\}$ form fourfold degenerate eigenstates which are dispersionless along another BZ boundary satisfying $k_x - k_y = \pi$.

When the hopping processes between the second and third nearest-neighbor sites are included, the diagonal line states become dispersive. Thus dispersionless DLN can be spanned by the diagonal line states only under a certain limited condition, which, in the present problem, corresponds to the case when the rotation angle of an oxygen octahedron reaches the critical value $\theta_c \sim 16°$. The Hamiltonian describing the hopping amplitudes between the second (t_2) and the third (t_3) nearest-neighbor sites is given by

$$\hat{H}_{23} = t_2 \sum_{\langle\langle \boldsymbol{r}, \boldsymbol{r}' \rangle\rangle, \sigma} \left[c_\sigma(\boldsymbol{r})^\dagger c_\sigma(\boldsymbol{r}') + \text{H.c.} \right]$$
$$+ t_3 \sum_{\langle\langle\langle \boldsymbol{r}, \boldsymbol{r}' \rangle\rangle\rangle, \sigma} \left[c_\sigma^\dagger(\boldsymbol{r}) c_\sigma(\boldsymbol{r}') + \text{H.c.} \right], \quad (8)$$

which, in momentum space, gives rise to $\varepsilon_2(\mathbf{k}, \theta)$ and $\varepsilon_3(\mathbf{k}, \theta)$ in Eq. (4). By applying $\hat{H}_{23}$ to $|\Psi\rangle_{\ell_\alpha, \sigma}^\alpha$, we obtain

$$\hat{H}_{23} |\Psi\rangle_{\ell_\alpha, \sigma}^\alpha = (2t_3 - t_2) \left[|\Psi\rangle_{\ell_\alpha + 2, \sigma}^\alpha + |\Psi\rangle_{\ell_\alpha - 2, \sigma}^\alpha \right]$$
$$- 2t_2 |\Psi\rangle_{\ell_\alpha, \sigma}^\alpha. \quad (9)$$

Thus, for $|\Psi\rangle^{\alpha}_{\ell_{\alpha},\sigma}$ to be the eigenstate of $\hat{H}_{23}$, the condition $t_2 = 2t_3$ should be satisfied. In fact, this is an identical condition to obtain θ_c at which the dispersionless DLN appears on the BZ boundary. When further neighbor hopping processes are included additionally, diagonal line states may not be localized eigenstates anymore, but the suitable linear combination of them can recover compact localized states spanning a flat zone-boundary DLN. Therefore a zone-boundary DLN is generally expected to exist as along as the symmetry of the system is maintained and there is enough of a number of control parameters such as the rotation angle of oxygen octahedra.

It is worthwhile to note that a pair of neighboring diagonal line states can construct the degenerate eigenstates of a zigzag-shaped chain shown in Fig. 4(f), which consist of the aforementioned zone-boundary Dirac point of the 1D Peierls system. This again supports the idea of viewing the distorted 2D lattice as stacking 1D zigzag-shaped chains with glide symmetry.

VI. MAGNETIC INSTABILITY DRIVEN BY THE DISPERSIONLESS DLN

Here we discuss the physical consequence induced by the dispersionless DLN on the BZ boundary. Let us note that in a polyacetylene chain with zigzag-type deformation at its critical point, the static susceptibility diverges logarithmically at the momentum $q = 0$ (modulo a reciprocal lattice vector) signaling a sublattice symmetry breaking. Although the nature of the resulting ground state depends on the effective interaction, the sublattice symmetry breaking always accompanies the breaking of the glide mirror that otherwise protects the Dirac point, leading to a gapped phase with lower energy. A similar idea can be applied to a 2D Peierls system driven by a flat zone-boundary DLN. Due to the perfect Fermi surface nesting from the dispersionless DLN, the uniform static susceptibility with the momentum $q = 0$ (modulo a reciprocal lattice vector) diverges logarithmically. An order parameter breaking the glide mirror symmetry can lift the degeneracy of DLN leading to a gapped insulator with lower energy. In the case of Sr_2IrO_4, its ground state is known to be a Neel-type AFM with in-plane spin canting (in-plane canted AFM). In the following, we examine the magnetic instability of this system focusing on the role of the zone-boundary DLN whose bandwidth can be controlled by varying the rotation angle θ of oxygen octahedra.

Previous theoretical studies have shown that the lattice model for a monolayer composed of $J_{eff} = 1/2$ states cannot capture the spin anisotropy of the system [7,22]. Thus, to obtain the in-plane canted AFM ground state numerically, we consider the 3D structure with the unit cell comprised of four layers. Let us note that, as long as the glide symmetries are preserved, the almost flat DLN can still appear even in the presence of interlayer coupling, which merely renormalizes the critical angle at which the zone-boundary DLN becomes dispersionless. We determine the magnetic ground state derived from the DLN and the relevant phase diagram by studying both the RPA-type spin susceptibility and the self-consistent mean field theory.

The general form of the spin susceptibility is given by $\chi^{ij}_{\alpha\alpha',ll'}(\mathbf{q}) = -\int_0^{\beta} d\tau \langle S^i_{\alpha l}(\mathbf{q}, \tau) S^j_{\alpha' l'}(-\mathbf{q}, 0)\rangle$ where the spin operator is defined as $S^i_{\alpha l}(\mathbf{q}, \tau) = \sum_{\mathbf{p}} c^{\dagger}_{\mathbf{p},\alpha l}(\tau)[\sigma^i]c_{\mathbf{p}+\mathbf{q},\alpha l}(\tau)$. Here α, α' and l, l' indicate the sublattice and layer indices, respectively. To distinguish the two candidate ground states, the in-plane canted AFM and the c-axis collinear AFM, we have computed the spin susceptibility $\chi^{+-}_{AFM}(\mathbf{q})$ and $\chi^{zz}_{AFM}(\mathbf{q})$ at the momentum $\mathbf{q}$ considering the staggered spin operator $S'^i = S^i_A - S^i_B$ in the unit cell. As shown in Fig. 5(b), the spin susceptibility develops a peak at $\mathbf{q} = (0, 0)$. The magnitude of the spin susceptibility for in-plane AFM ordering is larger than that of c-axis AFM ordering as indicated in Fig. 5(c), which agrees with the experimental results [17]. Upon varying the rotation angle of IrO_6 octahedron, the susceptibility at $\mathbf{q} = 0$ rapidly grows and reaches its maximum at a critical angle where energy spectrum along the BZ boundary becomes almost flat [Fig. 5(d)]. Using the RPA-corrected spin susceptibility $\chi^{RPA} = \frac{\chi^0}{1-U\chi^0}$, we can determine the critical value of the Coulomb interaction U_c from the condition that χ^{RPA} diverges at $U = U_c$, which is summarized in the phase diagram shown in Fig. 5(e).

Additionally, to confirm the magnetic ordering pattern suggested by the spin susceptibility, we have performed a self-consistent mean field calculation of a Hubbard-type model Hamiltonian with on-site repulsion: $H = H_t + H_U$ where H_t is a 16×16 tight-binding Hamiltonian including the sublattice, $J_{eff} = 1/2$ pseudospins, and the layer degrees of freedom. The mean-field decoupling of the Hubbard interaction is implemented as $H_U = U \sum_i n_{i\uparrow} n_{i\downarrow} \rightarrow -U \sum_i (2\langle \mathbf{S}\rangle_i \cdot \mathbf{S}_i - \langle \mathbf{S}_i \rangle^2)$ with $\langle \mathbf{S}_i \rangle = \langle \sum_{\sigma,\sigma'} c^{\dagger}_{i\sigma} \frac{\sigma_{\sigma\sigma'}}{2} c_{i\sigma'} \rangle \equiv \mathbf{m}_i$. We determine the magnetic ordering pattern by computing the order parameter $\mathbf{m}^A = (m^A_x, m^A_y, m^A_z)$ for sublattice A and $\mathbf{m}^B = (m^B_x, m^B_y, m^B_z)$ for sublattice B in the bottom layer self-consistently. Adopting the "up-down-down-up" type interlayer spin ordering pattern confirmed in previous studies [7,25], the order parameters in the other three layers are chosen accordingly. The resulting phase diagram is demonstrated in Fig. 5(e). The mean field theory shows that the critical interaction strength U at which the phase transition occurs becomes minimal when the rotation angle reaches the critical value $\theta = 16°$. As shown in Fig. 5(e), U_c determined from χ^{RPA} agrees well with the result from the self-consistent mean field theory, which confirms that the in-plane canted AFM ground state in Sr_2IrO_4 manifests itself as a consequence of 2D Peierls instability.

Let us note that in Ba_2IrO_4 where Sr is replaced by Ba, the ground state is an AFM insulator although there is no rotation distortion ($\theta = 0$) [26]. In this case, since the space group of the system without rotational distortion is symmorphic, one may expect that our theory based on the zone-boundary Dirac line node cannot be applied. However, let us stress that this is not the case. If we plot the band structure by using the same doubled unit cell, one can still observe the zone-boundary Dirac line node, and the magnetic instability of the system can still be described by using the same theoretical framework. The physical property of the system is independent of the unit cell choice. The existence of the zone-boundary DLN in Ba_2IrO_4 is confirmed by the tight-binding approach [see Fig. 3(b)] as well as DFT calculations where $\sqrt{2} \times \sqrt{2}$ unit cell is used (see Appendix C 4).
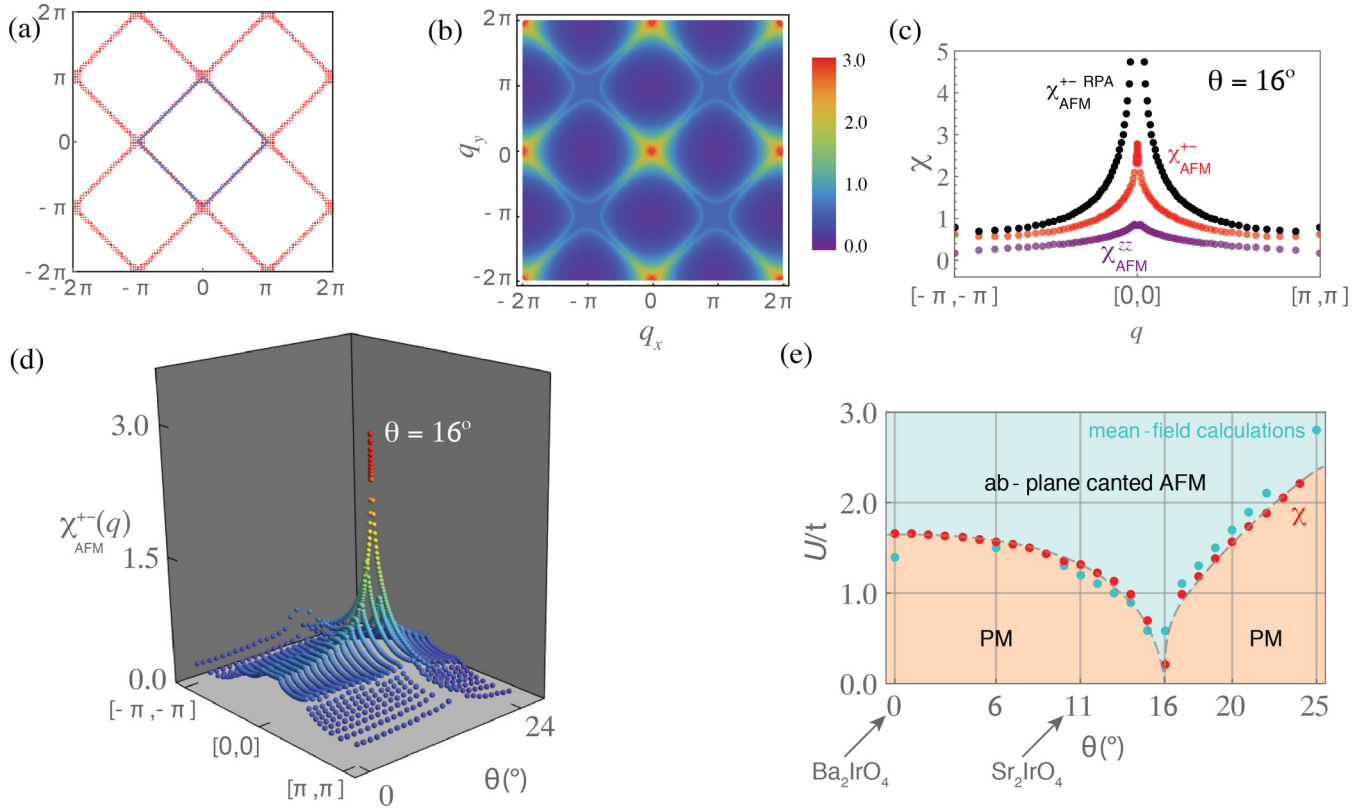
FIG. 5. Static susceptibility at the critical angle and the generic phase diagram. (a) The Fermi surface when the dispersion of the Dirac line node (DLN) along the Brillouin zone (BZ) boundary becomes flat. (b) Susceptibility $\chi_{AFM}^{+-}(q)$ has a sharp peak at $\mathbf{q} = (0, 0)$ modulo a reciprocal lattice vector. (c) The comparison of χ_{AFM}^{+-} and χ_{AFM}^{zz}. The susceptibility with RPA correction is shown by the black dashed line. (d) The susceptibility $\chi_{AFM}^{+-}(q)$ as a function of the rotation angle θ, which diverges logarithmically at the critical angle $\theta = 16°$. (e) The phase diagram in the $(\theta, U/t)$ plane where U indicates the local Coulomb repulsion and t indicates the nearest neighbor hopping amplitudes. Here the red (blue) dot denotes the critical point obtained by the RPA susceptibility (the self-consistent mean field study). At the critical angle the system shows a magnetic instability even in the presence of an infinitesimally small interaction.

In particular, one can also observe the flattening of the DLN as θ is increased artificially, although the real system with $\theta = 0$ can develop AFM state due to the relatively strong U. This clearly shows that the Dirac line node based AFM mechanism is still valid in the Ba_2IrO_4 system as well.

VII. DOMAIN WALL SOLITONS

The emergence of zero-dimensional (0D) soliton modes localized at a domain wall (DW) is a hallmark of 1D Peierls systems, which is normally described by the Su-Schrieffer-Heeger (SSH) model [27]. As a natural extension, in 2D Peierls systems, one can expect emerging 1D soliton modes localized along a DW, which can be considered as the coupled 0D soliton modes stacked along the DW direction. To demonstrate this idea, we have studied the energy spectrum of a configuration at the critical rotation angle with a magnetic DW between two canted AFM domains with the net ferromagnetic moments along the $+Y$ and $-Y$ directions, respectively, as shown in Fig. 6(a). For simplicity, we first have considered a "smooth wall" in which the magnitudes of local magnetic moments are smoothly scaled down to zero as we approach the DW from the bulk region whereas the direction of spins in each domain is fixed. As shown in Figs. 6(b) and 6(c), one

can clearly observe two in-gap states as the 1D soliton modes localized along the DW. When the local magnetic moment at the DW (m_{DW}) is zero, the in-gap states appear exactly at the zero energy, which are dispersionless due to the same reason as the localized chain states appear. On the other hand, as m_{DW} increases, the two in-gap states couple and develop dispersion with a small gap between them. However, even when m_{DW} becomes as big as the local magnetic moment in the bulk, the gap between the soliton modes is ten times smaller than the bulk gap as shown in Fig. 6(d). Both the lattice model study and the low energy effective Hamiltonian analysis consistently show that the in-gap states localized at the DW share the same origin as the DW soliton predicted in the original SSH model as discussed in detail in Appendix H.

To confirm the robustness of the in-gap states independent of the detailed structure around the DW, we have studied the energy spectra of various DW configurations considering different DW direction and changing the orientation of the net ferromagnetic moment as shown in Figs. 6(e) and 6(g). For instance, allowing the rotation of spin directions around the DW, we have considered the Neel-type and Bloch-type DWs, both of which possess similar in-gap states. (See Appendix H 4 b and H 4 c.) When the DW is parallel to either the x or y direction, the in-gap states appear more dispersive as compared to the case of DWs parallel to the X or Y directions
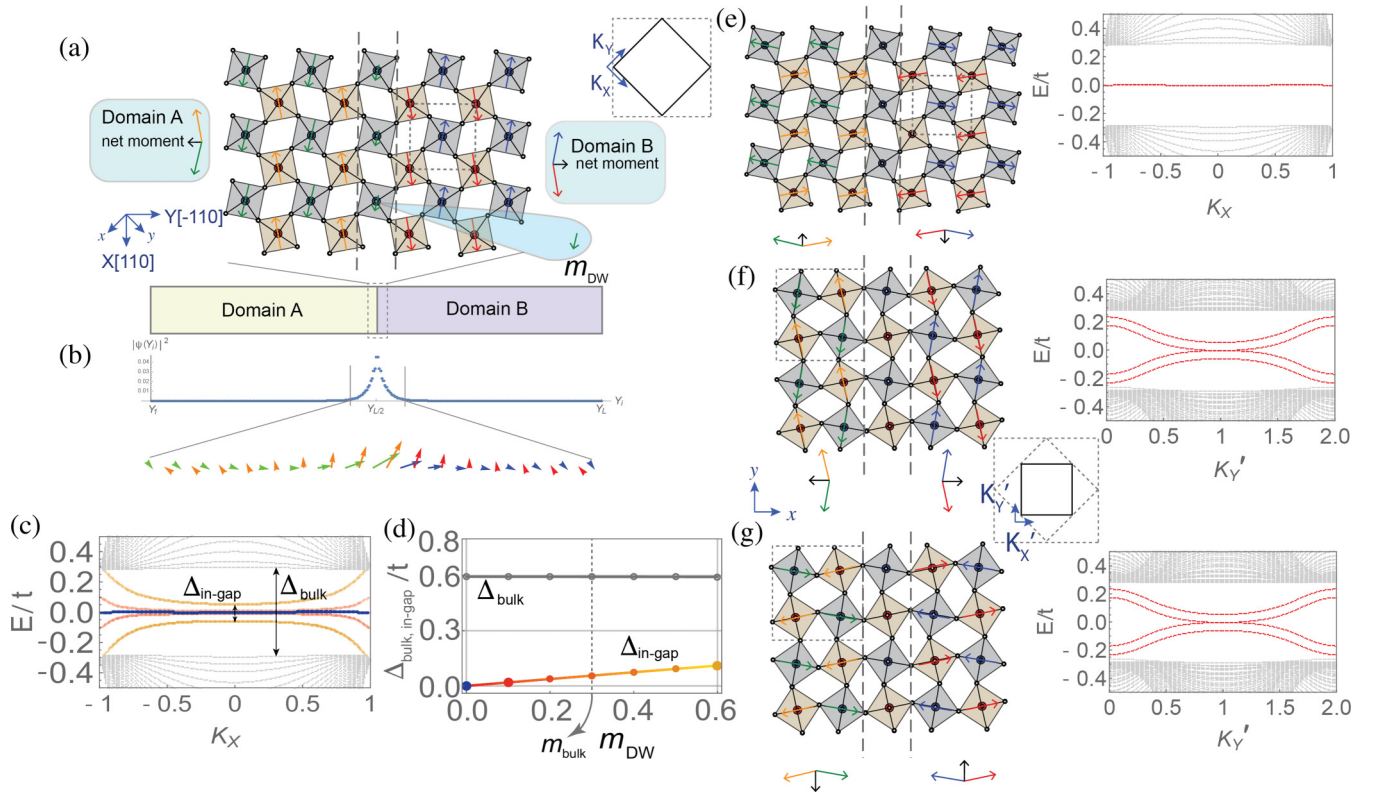
FIG. 6. One-dimensional (1D) soliton modes along magnetic domain walls (DWs). (a) A schematic figure showing a 1D DW parallel to the X axis. The green and orange arrows indicate the magnetic moments in the domain A with the net magnetic moment pointing perpendicular to the DW. The red and blue arrows are the magnetic moments in the domain B with the net magnetic moment opposite to that of the domain A. (b) Spatial distribution (along the Y direction) of the wave function amplitude of a soliton state localized at the DW. (c) Energy spectrum of the system shown in (a). The orange, red, and blue lines show the dispersion of the in-gap states when the local magnetic moment at the DW, m_{DW}, is 0.6, 0.1, 0, respectively. (d) The bulk gap (Δ_{bulk}) vs the gap between in-gap states ($\Delta_{in\text{-}gap}$) as a function of the magnitude of m_{DW}. (e) A DW configuration and the relevant energy spectrum when the net magnetic moment in each domain is parallel to the DW. (f), (g) A DW configuration and the relevant energy spectrum when the DW is parallel to the x axis and the net magnetic moment is perpendicular to the DW (f) and parallel to the DW (g), respectively.

as shown in Figs. 6(f) and 6(g). In all cases, it is found that the in-gap states localized at the DW are robust and well separated from the bulk states, thus they are detectable through local conductivity measurements [28,29].

VIII. DISCUSSION

We conclude with the discussion about experimental evidence supporting the presence of zone-boundary DLN. According to the recent ARPES study of La doped iridates $La_xSr_{2-x}IrO_4$, a collapse of the charge gap due to electron doping results in a paramagnetic metallic state with nodal fermionic excitations [30]. Since electron doping shifts the position of the Fermi level, which weakens the instability associated with the DLN, it is natural to expect the recovery of the zone-boundary DLN as long as two orthogonal glide symmetries remain intact in the doped paramagnetic state. If one of the two glide mirrors is broken, for instance due to the presence of another nonmagnetic order parameter, the zone-boundary DLN can be deformed to Dirac points protected by the remaining glide mirror [31]. Overall, the relatively weak dispersion of the zone-boundary DLN in Sr_2IrO_4 makes the critical interaction U_c small, thus the recovery of the

paramagnetic semimetal with DLN requires a huge reduction of the effective Coulomb repulsion through carrier doping [32].

On the other hand, in Sr_2RhO_4 where Ir^{4+} is replaced by Rh^{4+} having five valence electrons in $4d$ orbitals, a paramagnetic metallic state is realized due to the weak electron correlation and large effective bandwidth. Previous ARPES study and first-principles calculation consistently show the presence of zone-boundary DLN [33–35]. To induce an instability by controlling the rotation angle of RhO_6 octahedra, either by applying electric field or chemical doping would be an intriguing topic for future studies. By means of DFT calculations, it can be shown that the bandwidth of the zone-boundary DLN in Sr_2RhO_4 also changes as a function of the rotational angle. It is minimized by a suitable choice of the rotational angle as shown in Appendix C 3. It is worthwhile to mention that the position of the DLN is deviated from the Fermi level due to the overlap with other dispersive bands resulting in a large effective bandwidth in total. As a consequence, the instability of the DLN is compromised and the system remains the paramagnetic metallic state in Sr_2RhO_4.

The recent second harmonic generation study as well as the neutron diffraction measurements [9,36,37] indicate that the

crystal structure of Sr_2IrO_4 is described by space group $I4_1/a$, which is different from the nonsymmorphic group $I4_1/acd$. The modification of the crystal structure is associated with the staggered tetragonal distortion of oxygen octahedron such that the ratio of the out of plane Ir-O bond length and the in-plane Ir-O bond length at the two Ir sublattice sites are different by 0.1 percent. Even though such a small tetragonal distortion is enough to generate superlattice peaks for structure analysis, it hardly affects the electronic structure and thus the instability of the DLN as well. The DFT band structure calculations shows that the energy splitting due to the staggered tetragonal distortion is indeed negligible. (For details, see Appendix D.)

Finally, let us note that our theory can help resolve the controversy about the origin of the AFM in Sr_2IrO_4, which is typically ascribed either to the Slater mechanism or to the Mott mechanism [38]. The in-plane AFM ordering doubles the unit cell and it is accompanied by the insulating behavior, supporting the Slater mechanism. On the other hand, the fact that the unit-cell doubling happens above the Neel temperature and the insulating behavior is accompanied by significant band renormalization supports the Mott mechanism. According to our theory, the correct way to describe the AFM is to take into account both viewpoints at the same time. Namely, the doubling of the unit cell due to the lattice distortion generates symmetry protected zone-boundary DLNs which provide a platform for magnetic instability. Then subsequent flattening of the DLN enhances the effect of Mott correlation, which eventually drives the AFM ground state. We believe that our theory reveals a clear microscopic picture to understand the interplay between the symmetry protected band structure and the Mott correlation, leading to the AFM ground state in Sr_2IrO_4. The intricate balance among the spin-orbit coupled band structure, lattice symmetry, and electron correlation underlies the magnetic instability of Sr_2IrO_4, which would provide a new perspective to envision various the spin-orbit coupled complex correlated electron systems in general.

APPENDIX A: ROLE OF MULTIPLE NONSYMMORPHIC SYMMETRIES

To describe the symmetry of Sr_2IrO_4, let us use the $\sqrt{2} \times \sqrt{2}$ unit cell from the beginning. Namely, there are two atoms in a unit cell. Then we define a unit translation along x and

y directions in a way that the first Brillouin zone is defined as $-\pi \leqslant k_x, k_y \leqslant \pi$. Namely, here x and y coordinates correspond to the conventional a and b coordinates in previous literatures.

1. Point group symmetries

The point group symmetry of the system is generated by inversion P and two glide mirrors G_x and G_y. Including time-reversal symmetry, space-time coordinates transforms as in the following way:

$$
\begin{aligned}
T &: (x, y, t) \rightarrow (x, y, -t) \times i\sigma_y, \\
P &: (x, y, t) \rightarrow (-x, -y, t), \\
G_x &: (x, y, t) \rightarrow \left(-x + \tfrac{1}{2}, y + \tfrac{1}{2}, t\right) \times i\sigma_x, \\
G_y &: (x, y, t) \rightarrow \left(x + \tfrac{1}{2}, -y + \tfrac{1}{2}, t\right) \times i\sigma_y. \quad \text{(A1)}
\end{aligned}
$$

Equivalently, one can use two twofold screw rotations $S_x \equiv G_x P$ and $S_y \equiv G_y P$ instead of $G_{x,y}$. $S_{x,y}$ transforms the space-time coordinate as

$$
\begin{aligned}
S_x &: (x, y, t) \rightarrow \left(x + \tfrac{1}{2}, -y + \tfrac{1}{2}, t\right) \times i\sigma_x, \\
S_y &: (x, y, t) \rightarrow \left(-x + \tfrac{1}{2}, y + \tfrac{1}{2}, t\right) \times i\sigma_y. \quad \text{(A2)}
\end{aligned}
$$

2. Dirac line nodes on the Brillouin zone boundary

Here we prove the symmetry protection of the Dirac line nodes on $k_x = \pi$ or $k_y = \pi$ lines. First, let us consider the $k_x = \pi$ line. On this line, the system is invariant under PT, G_x, S_y. Thus every band on the $k_x = \pi$ line can be labeled either by G_x eigenvalue or by S_y eigenvalues. The G_x and S_y eigenvalues can be simultaneously determined only if these two symmetries commute. In any case, let us use G_x eigenvalues to label bands on the $k_x = \pi$ line. From $G_x^2 = -e^{ik_y}$ we find that G_x has two eigenvalues $n_{x,\pm}(k_y) = \pm i e^{i\frac{1}{2}k_y}$. Then one can define the G_x eigenstates in the following way.

$$
G_x |n_{x,\pm}(k_y)\rangle = n_{x,\pm}(k_y)|n_{x,\pm}(k_y)\rangle \quad \text{(A3)}
$$

which can be satisfied on the $k_x = 0$ and $k_x = \pi$ lines.

To understand the band connection on the $k_x = \pi$ line, it is useful to examine the commutation relation between PT, G_x, S_y. Again, these symmetries transform the space time coordinates as

$$
\begin{aligned}
PT &: (x, y, t) \rightarrow (-x, -y, -t) \times i\sigma_y, \\
G_x &: (x, y, t) \rightarrow \left(-x + \tfrac{1}{2}, y + \tfrac{1}{2}, t\right) \times i\sigma_x, \\
S_y &: (x, y, t) \rightarrow \left(-x + \tfrac{1}{2}, y + \tfrac{1}{2}, t\right) \times i\sigma_y. \quad \text{(A4)}
\end{aligned}
$$

Their product transforms the space-time coordinates as

$$
\begin{aligned}
PTG_x &: (x, y, t) \rightarrow \left(x - \tfrac{1}{2}, -y - \tfrac{1}{2}, -t\right) \times (i\sigma_y)(-i\sigma_x), \\
G_xPT &: (x, y, t) \rightarrow \left(x + \tfrac{1}{2}, -y + \tfrac{1}{2}, -t\right) \times (i\sigma_x)(i\sigma_y), \\
PTS_y &: (x, y, t) \rightarrow \left(x - \tfrac{1}{2}, -y - \tfrac{1}{2}, -t\right) \times (i\sigma_y)(i\sigma_y), \\
S_yPT &: (x, y, t) \rightarrow \left(x + \tfrac{1}{2}, -y + \tfrac{1}{2}, -t\right) \times (i\sigma_y)(i\sigma_y), \\
S_yG_x &: (x, y, t) \rightarrow (x, y + 1, t) \times (i\sigma_y)(i\sigma_x), \\
G_xS_y &: (x, y, t) \rightarrow (x, y + 1, t) \times (i\sigma_x)(i\sigma_y), \quad \text{(A5)}
\end{aligned}
$$

which gives rise to the following commutation relations

$$PTG_x = e^{ik_x - ik_y}G_xPT,$$

$$PTS_y = e^{ik_x - ik_y}S_yPT,$$

$$S_yG_x = -G_xS_y. \tag{A6}$$

This commutation relation is valid in the whole momentum space.

Now we again focus on the $k_x = \pi$ line on which we have

$$PTG_x = -e^{-ik_y}G_xPT,$$

$$PTS_y = -e^{-ik_y}S_yPT, \tag{A7}$$

$$S_yG_x = -G_xS_y,$$

thus we see that G_x and S_y cannot be diagonalized simultaneously. First, let us compare G_x eigenvalues of $|n_{x,\pm}(k_y)\rangle$ and $PT|n_{x,\pm}(k_y)\rangle$. From Eq. (A7), we find

$$G_xPT|n_{x,\pm}(k_y)\rangle = -e^{ik_y}PTG_x|n_{x,\pm}(k_y)\rangle$$

$$= -e^{ik_y}PT\left[\pm ie^{i\frac{1}{2}k_y}|n_{x,\pm}(k_y)\rangle\right]$$

$$= \pm ie^{i\frac{1}{2}k_y}\left[PT|n_{x,\pm}(k_y)\rangle\right]$$

$$= n_{x,\pm}(k_y)\left[PT|n_{x,\pm}(k_y)\rangle\right] \tag{A8}$$

thus a Kramers pair $|n_{x,\pm}(k_y)\rangle$ and $PT|n_{x,\pm}(k_y)\rangle$ have the same G_x eigenvalues.

Now we compare G_x eigenvalues of $|n_{x,\pm}(k_y)\rangle$ and $S_y|n_{x,\pm}(k_y)\rangle$. From the anticommutation relation between S_y and G_x, it is obvious that

$$G_xS_y|n_{x,\pm}(k_y)\rangle = -[n_{x,\pm}(k_y)]S_y|n_{x,\pm}(k_y)\rangle$$

$$= [n_{x,\mp}(k_y)]S_y|n_{x,\pm}(k_y)\rangle \tag{A9}$$

thus $|n_{x,\pm}(k_y)\rangle$ and $S_y|n_{x,\pm}(k_y)\rangle$ have different G_x eigenvalues. Since the system is invariant under PT, S_y, G_x on the $k_x = \pi$ line, the four states $|n_{x,\pm}(k_y)\rangle$ and $PT|n_{x,\pm}(k_y)\rangle$ and $S_y|n_{x,\pm}(k_y)\rangle$ and $PTS_y|n_{x,\pm}(k_y)\rangle$ with G_x eigenvalues $n_{x,\pm}(k_y)$, $n_{x,\pm}(k_y)$, $n_{x,\mp}(k_y)$, $n_{x,\mp}(k_y)$, respectively, are all degenerate with the same energy, thus there should be a Dirac line node with fourfold degeneracy on the $k_x = \pi$ line. One can perform similar analysis on the $k_y = \pi$ line, and thus the DLN spanning the full BZ boundary can be understood.

APPENDIX B: DETAILS OF HOPPING INTEGRALS IN TIGHT-BINDING HAMILTONIAN

The bandwidth control by varying the rotational angle of octahedron is important to examine the nesting induced instability in layered perovskite oxide systems. Here we explain how the hopping integrals in the tight-binding Hamiltonian in Eq. (4) are obtained. We use the Slater-Koster methods to derive the θ-dependent hopping integrals between spin-orbit coupled states of $|J_{\text{eff}} = \pm\frac{1}{2}\rangle = \frac{1}{\sqrt{3}}(|d_{yz} \mp s\rangle \pm i|d_{zx} \mp s\rangle \pm |d_{xy} \pm s\rangle)$, where s refers to the spin. It is based on the idea that the hopping integrals can be decomposed into several hopping elements such as $V_{dd\pi}$, $V_{dd\delta}$, $V_{dd\sigma}$ in the d-orbitals basis and can be parameterized with respect to the relative displacement between two orbitals. The relative displacement is then adjusted by the amount of the angle for rotational distortion θ. (See also Appendix B 1). Accordingly, the explicit

form of hopping integrals in (4) are

$$2t_1 = \frac{1}{12}[12V_{dd\pi} - V_{dd\delta} - 3V_{dd\sigma}] + \frac{2}{3}[V_{dd\pi} + V_{dd\delta}]\cos 2\theta$$

$$- \frac{1}{12}[4V_{dd\pi} - V_{dd\delta} - 3V_{dd\sigma}]\cos 4\theta,$$

$$2t_{1d} = \frac{2}{3}[V_{dd\pi} + V_{dd\delta}]\sin 2\theta,$$

$$4t_2 = \frac{1}{2}[4V_{dd\pi} + 3V_{dd\delta} + V_{dd\sigma}]$$

$$- \frac{1}{6}[4V_{dd\pi} - V_{dd\delta} - 3V_{dd\sigma}]\cos 4\theta,$$

$$2t_3 = \frac{1}{4}[4V_{dd\pi n} + 3V_{dd\delta n} + V_{dd\sigma n}]$$

$$+ \frac{1}{12}[4V_{dd\pi n} - V_{dd\delta n} - 3V_{dd\sigma n}]\cos 4\theta. \tag{B1}$$

The rotational angle dependence $\sim\cos 4\theta$ results from the intraorbital hybridization between d_{xy}-orbitals. The rotational angle dependence $\sim\cos 2\theta$ in t_1 describes the intraorbital hybridization within d_{yz} orbitals or d_{zx} orbitals whereas the rotational angle dependence $\sim\sin 2\theta$ in t_{1d} describes the interorbital hybridization between d_{yz} orbitals and d_{zx} orbitals. The hopping elements between nearest neighbor sites are chosen as $(V_{dd\pi}, V_{dd\delta}, V_{dd\sigma}) = (1, -0.25, -1.5)$ and those for the next nearest neighbor sites are $(V_{dd\pi n}, V_{dd\delta n}, V_{dd\sigma n}) = l \times (V_{dd\pi}, V_{dd\delta}, V_{dd\sigma})$ with $l = 0.07$. The factor l reflects the reduction of hopping integral with respect to the distance. Naively, the reduction factor has to be chosen as $l = (1/2)^5 \approx 0.0312$, but considering the results from *ab initio* calculations [7], we have used $l = 0.07$.

1. Slater-Koster parameter method

We use Slater-Koster parameters within the same sublattice τ as follows:

$$\langle d_{yz,0,\tau}|H|d_{yz,i,\tau}\rangle = V_{dd\pi}\cos^2(\theta - \phi) + V_{dd\delta}\sin^2(\theta - \phi),$$

$$\langle d_{zx,0,\tau}|H|d_{zx,i,\tau}\rangle = V_{dd\delta}\cos^2(\theta - \phi) + V_{dd\pi}\sin^2(\theta - \phi),$$

$$\langle d_{xy,0,\tau}|H|d_{xy,i,\tau}\rangle = V_{dd\pi}\cos^2(2(\theta - \phi))$$

$$+ V_{dd\sigma}\sin^2(2(\theta - \phi)). \tag{B2}$$

The Slater-Koster parameters depend on the rotation angle θ and relative displacement angle ϕ between two adjacent orbitals where $d_{\lambda,0}$ orbital locates at the origin and $d_{\lambda,i}$ orbital at $\mathbf{r}_i = (x_i, y_i)$. Thus ϕ is defined by

$$(\cos\phi, \sin\phi) = (x_i, y_i)/\sqrt{x_i^2 + y_i^2}. \tag{B3}$$

Similarly, we have the Slater-Koster parameters between different sublattices τ and $\bar{\tau}$ which are given by

$$\langle d_{yz,0,\tau}|H|d_{yz,i,\bar{\tau}}\rangle = \langle d_{yz,0,\bar{\tau}}|H|d_{yz,i,\tau}\rangle$$

$$= V_{dd\pi}\cos(\theta - \phi)\cos(\theta + \phi)$$

$$- V_{dd\delta}\sin(\theta - \phi)\sin(\theta + \phi),$$

$$\langle d_{zx,0,\tau}|H|d_{zx,i,\bar{\tau}}\rangle = \langle d_{zx,0,\bar{\tau}}|H|d_{zx,i,\tau}\rangle$$

$$= V_{dd\delta}\cos(\theta - \phi)\cos(\theta + \phi)$$

$$- V_{dd\pi}\sin(\theta - \phi)\sin(\theta + \phi),$$

$$\langle d_{xy,0,\tau}|H|d_{xy,i,\bar{\tau}}\rangle = \langle d_{xy,0,\bar{\tau}}|H|d_{xy,i,\tau}\rangle$$

$$= V_{dd\pi}\cos(2(\theta - \phi))\cos(2(\theta + \phi))$$

$$- V_{dd\sigma}\sin(2(\theta - \phi))\sin(2(\theta + \phi)). \tag{B4}$$

The collective rotation allows the hopping between different orbitals of d_{yz} and d_{zx} as follows:

$$
\begin{aligned}
\langle d_{yz,0,\tau}|H|d_{zx,i,\overline{\tau}}\rangle &= -\langle d_{yz,0,\overline{\tau}}|H|d_{zx,i,\tau}\rangle \\
&= -V_{dd\pi}\cos(\theta-\phi)\sin(\theta+\phi) \\
&\quad - V_{dd\delta}\cos(\theta+\phi)\sin(\theta-\phi), \\
\langle d_{zx,0,\tau}|H|d_{yz,i,\overline{\tau}}\rangle &= -\langle d_{zx,0,\overline{\tau}}|H|d_{yz,i,\tau}\rangle \\
&= V_{dd\pi}\sin(\theta-\phi)\cos(\theta+\phi) \\
&\quad + V_{dd\delta}\cos(\theta-\phi)\sin(\theta+\phi).
\end{aligned} \tag{B5}
$$

2. Hamiltonian with interlayer hopping

The Hamiltonian with interlayer hopping reads

$$
H_{\mathbf{k},\theta}^{ll'} = \begin{pmatrix}
A_{\mathbf{k},\theta} & B_{\mathbf{k},\theta} & 0 & e^{ik_zc}C_{\mathbf{k},\theta}^{\dagger} \\
B_{\mathbf{k},\theta}^{\dagger} & A_{\mathbf{k},\theta} & C_{\mathbf{k},\theta} & 0 \\
0 & C_{\mathbf{k},\theta}^{\dagger} & A_{\mathbf{k},\theta} & B_{\mathbf{k},\theta} \\
e^{-ik_zc}C_{\mathbf{k},\theta} & 0 & B_{\mathbf{k},\theta}^{\dagger} & A_{\mathbf{k},\theta}
\end{pmatrix}, \tag{B6}
$$

where

$$
\begin{aligned}
A_{\mathbf{k},\theta} &= \varepsilon_{\mathbf{k},\theta}^a \tau^0\sigma^0 + \varepsilon_{\mathbf{k},\theta}^{ad}\tau^x\sigma^0 + \varepsilon_{\mathbf{k},\theta}^{ad'}\tau^y\sigma^z, \\
B_{\mathbf{k},\theta} &= \varepsilon_{\mathbf{k},\theta}^b \tau^0\sigma^0 + \varepsilon_{\mathbf{k},\theta}^{bd}\tau^x\sigma^0 + \varepsilon_{\mathbf{k},\theta}^{bz}\tau^y\sigma^z \\
&\quad + \varepsilon_{\mathbf{k},\theta}^{by}\tau^y\sigma^y + \varepsilon_{\mathbf{k},\theta}^{bx}\tau^y\sigma^x, \\
B_{\mathbf{k},\theta}^{\dagger} &= \varepsilon_{\mathbf{k},\theta}^b \tau^0\sigma^0 + \varepsilon_{\mathbf{k},\theta}^{bd}\tau^x\sigma^0 + \varepsilon_{\mathbf{k},\theta}^{bz}\tau^y\sigma^z \\
&\quad - \varepsilon_{\mathbf{k},\theta}^{by}\tau^y\sigma^y - \varepsilon_{\mathbf{k},\theta}^{bx}\tau^y\sigma^x, \\
C_{\mathbf{k},\theta} &= \varepsilon_{\mathbf{k},\theta}^c \tau^0\sigma^0 + \varepsilon_{\mathbf{k},\theta}^{cd}\tau^x\sigma^0 + \varepsilon_{\mathbf{k},\theta}^{cz}\tau^y\sigma^z \\
&\quad + \varepsilon_{\mathbf{k},\theta}^{cy}\tau^y\sigma^y + \varepsilon_{\mathbf{k},\theta}^{cx}\tau^y\sigma^x, \\
C_{\mathbf{k},\theta}^{\dagger} &= \varepsilon_{\mathbf{k},\theta}^c \tau^0\sigma^0 + \varepsilon_{\mathbf{k},\theta}^{cd}\tau^x\sigma^0 + \varepsilon_{\mathbf{k},\theta}^{cz}\tau^y\sigma^z \\
&\quad - \varepsilon_{\mathbf{k},\theta}^{cy}\tau^y\sigma^y - \varepsilon_{\mathbf{k},\theta}^{cx}\tau^y\sigma^x.
\end{aligned} \tag{B7}
$$

Here, τ^i and σ^i with $i = 0, x, y, z$ indicate the Pauli matrices acting on the sublattice spaces and $J_{\text{eff}} = 1/2$ spaces, respectively. To fully express Eq. (B6) with Pauli matrices, ρ^i and η^i are introduced without any physical meaning:

$$
\rho^0\eta^0 = \begin{pmatrix} 1 & 0 & 0 & 0 \\ 0 & 1 & 0 & 0 \\ 0 & 0 & 1 & 0 \\ 0 & 0 & 0 & 1 \end{pmatrix}, \ \rho^x\eta^0 = \begin{pmatrix} 0 & 1 & 0 & 0 \\ 1 & 0 & 0 & 0 \\ 0 & 0 & 0 & 1 \\ 0 & 0 & 1 & 0 \end{pmatrix},
$$

$$
(i\rho^y)\eta^0 = \begin{pmatrix} 0 & 1 & 0 & 0 \\ -1 & 0 & 0 & 0 \\ 0 & 0 & 0 & 1 \\ 0 & 0 & -1 & 0 \end{pmatrix}, \ \rho^x\eta^x = \begin{pmatrix} 0 & 0 & 0 & 1 \\ 0 & 0 & 1 & 0 \\ 0 & 1 & 0 & 0 \\ 1 & 0 & 0 & 0 \end{pmatrix},
$$

$$
\rho^y\eta^y = \begin{pmatrix} 0 & 0 & 0 & -1 \\ 0 & 0 & 1 & 0 \\ 0 & 1 & 0 & 0 \\ -1 & 0 & 0 & 0 \end{pmatrix}. \tag{B8}
$$

With this, we can write down Eq. (B6) as a compact form

$$
\begin{aligned}
H_{\mathbf{k},\theta}^{ll'} &= \varepsilon_{\mathbf{k},\theta}^a \tau^0\sigma^0\rho^0\eta^0 + \varepsilon_{\mathbf{k},\theta}^{ad}\tau^x\sigma^0\rho^0\eta^0 + \varepsilon_{\mathbf{k},\theta}^{ad'}\tau^y\sigma^z\rho^0\eta^0 \\
&\quad + \varepsilon_{\mathbf{k},\theta}^b\tau^0\sigma^0\rho^x\eta^0 + \varepsilon_{\mathbf{k},\theta}^{bd}\tau^x\sigma^0\rho^x\eta^0 + \varepsilon_{\mathbf{k},\theta}^{bz}\tau^y\sigma^z\rho^x\eta^0 \\
&\quad + \varepsilon_{\mathbf{k},\theta}^{by}\tau^y\sigma^y(i\rho^y)\eta^0 + \varepsilon_{\mathbf{k},\theta}^{bx}\tau^y\sigma^x(i\rho^y)\eta^0
\end{aligned}
$$

$$
\begin{aligned}
&\quad + \varepsilon_{\mathbf{k},\theta}^c\tau^0\sigma^0\rho^x\eta^x + \varepsilon_{\mathbf{k},\theta}^{cd}\tau^x\sigma^0\rho^x\eta^x + \varepsilon_{\mathbf{k},\theta}^{cz}\tau^y\sigma^z\rho^x\eta^x \\
&\quad + \varepsilon_{\mathbf{k},\theta}^{cy}\tau^y\sigma^y\rho^y\eta^y + \varepsilon_{\mathbf{k},\theta}^{cx}\tau^y\sigma^x\rho^y\eta^y.
\end{aligned} \tag{B9}
$$

The intralayer couplings are expressed as

$$
\begin{aligned}
\varepsilon_{\mathbf{k},\theta}^a &= 4t_2(\theta)\cos k_x\cos k_y + 2t_3(\theta)(\cos 2k_x + \cos 2k_y), \\
\varepsilon_{\mathbf{k},\theta}^{ad} &= 2t_1(\theta)(\cos k_x + \cos k_y), \\
\varepsilon_{\mathbf{k},\theta}^{ad'} &= 2t_{1d}(\theta)(\cos k_x + \cos k_y),
\end{aligned} \tag{B10}
$$

where the explicit expressions of $t_{1,1d,2,3}$ can be found in Eq. (B1). The interlayer couplings associated with $B_{\mathbf{k},\theta}$ are as follows:

$$
\begin{aligned}
\varepsilon_{\mathbf{k},\theta}^b &= 2[2V_{dd\delta z} + 3V_{dd\pi z} + V_{dd\sigma z} \\
&\quad + (V_{dd\delta z} - V_{dd\pi z})\cos 4\theta]\cos(k_x + k_y)/2, \\
\varepsilon_{\mathbf{k},\theta}^{bd} &= [V_{dd\sigma z} - V_{dd\pi z} + 2(V_{dd\delta z} + V_{dd\pi z})\cos 2\theta \\
&\quad + (V_{dd\pi z} + V_{dd\sigma z})\cos(4\theta)]\cos(k_x - k_y)/2, \\
\varepsilon_{\mathbf{k},\theta}^{bz} &= \tfrac{2}{3}[V_{dd\delta z} - V_{dd\pi z} + (V_{dd\delta z} + V_{dd\pi z})\sin 2\theta] \\
&\quad \times \cos(k_x - k_y)/2, \\
\varepsilon_{\mathbf{k},\theta}^{by} &= \tfrac{1}{24}[2V_{dd\delta z} - 2V_{dd\pi z} + (V_{dd\delta z} - 4V_{dd\pi z} \\
&\quad + 3V_{dd\sigma z})\cos 2\theta]\sin(k_x - k_y)/2, \\
\varepsilon_{\mathbf{k},\theta}^{bx} &= \tfrac{1}{24}[-2V_{dd\delta z} + 2V_{dd\pi z} + (V_{dd\delta z} - 4V_{dd\pi z} \\
&\quad + 3V_{dd\sigma z})\cos 2\theta]\sin(k_x - k_y)/2.
\end{aligned} \tag{B11}
$$

The interlayer couplings associated with $C_{\mathbf{k},\theta}$ are as follows:

$$
\begin{aligned}
\varepsilon_{\mathbf{k},\theta}^c &= 2[2V_{dd\delta z} + 3V_{dd\pi z} + V_{dd\sigma z} \\
&\quad + (V_{dd\delta z} - V_{dd\pi z})\cos 4\theta]\cos(k_x - k_y)/2, \\
\varepsilon_{\mathbf{k},\theta}^{cd} &= [V_{dd\sigma z} - V_{dd\pi z} + 2(V_{dd\delta z} + V_{dd\pi z})\cos 2\theta \\
&\quad + (V_{dd\pi z} + V_{dd\sigma z})\cos(4\theta)]\cos(k_x + k_y)/2, \\
\varepsilon_{\mathbf{k},\theta}^{cz} &= \tfrac{2}{3}[V_{dd\delta z} - V_{dd\pi z} + (V_{dd\delta z} + V_{dd\pi z})\sin 2\theta] \\
&\quad \times \cos(k_x + k_y)/2, \\
\varepsilon_{\mathbf{k},\theta}^{cy} &= \tfrac{1}{24}[2V_{dd\delta z} - 2V_{dd\pi z} - (V_{dd\delta z} - 4V_{dd\pi z} \\
&\quad + 3V_{dd\sigma z})\cos 2\theta]\sin(k_x + k_y)/2, \\
\varepsilon_{\mathbf{k},\theta}^{cx} &= \tfrac{1}{24}[-2V_{dd\delta z} + 2V_{dd\pi z} - (V_{dd\delta z} - 4V_{dd\pi z} \\
&\quad + 3V_{dd\sigma z})\cos 2\theta]\sin(k_x + k_y)/2.
\end{aligned} \tag{B12}
$$

The hopping elements between interlayer sites are chosen as $(V_{dd\pi z}, V_{dd\delta z}, V_{dd\sigma z}) = l * (1, -0.25, -1.5)$, where $l = 0.04$.

APPENDIX C: FIRST-PRINCIPLES CALCULATIONS

Our electronic structure calculations were based on density-functional theory within the local density approximation (LDA) as implemented in Elk code [39]. For the exchange-correlation energy part of the LDA functional, we used the Perdew-Zunger parametrization of the Ceperly-Alder data [40]. Spin-orbit coupling (SOC) was included in the second-variational scheme. Brillouin zone integrations were performed using $6 \times 6 \times 3$ grid sampling during the self-consistent calculations.
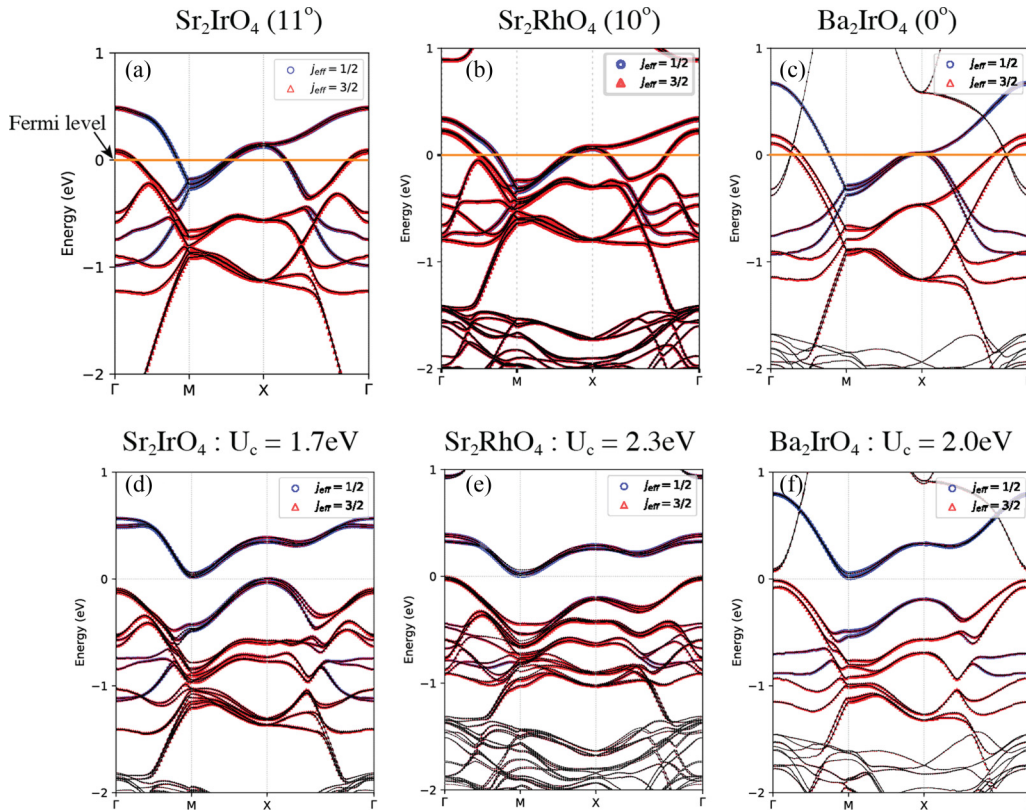
FIG. 7. (a)–(c) The DFT+SOC calculations for Sr_2IrO_4, Sr_2RhO_4, and Ba_2IrO_4 with rotational angles from experimental data. The orange line indicates the Fermi level. (d)–(f) The DFT+SOC+U calculations for Sr_2IrO_4, Sr_2RhO_4, and Ba_2IrO_4 with rotational angles from experimental data. The critical U for Sr_2IrO_4, Sr_2RhO_4, and Ba_2IrO_4 are $U_c = 1.7$ eV, 2.3 eV, and 2.0 eV, respectively.

1. DFT band structure calculations

First, we provide the DFT calculations for Sr_2IrO_4, Sr_2RhO_4, and Ba_2IrO_4 with rotational angles from experimental data. The rotation angles for Sr_2IrO_4, Sr_2RhO_4, and Ba_2IrO_4 are $11°$, $10°$, and $0°$, respectively. To compare the magnetic instability in these systems, one needs to carefully take into account the Coulomb interaction U and the influence of additional bands on the Fermi level together with the zone-boundary Dirac line nodes. The paramagnetic band structures are determined by DFT+SOC calculations, and the critical U for metal-insulator transition is obtained by DFT+SOC+U calculations as shown in Fig. 7. One peculiar property of the Sr_2RhO_4 paramagnetic band structure compared to that of Sr_2IrO_4 is that the $J_{eff} = 3/2$ states as well as the $J_{eff} = 1/2$ states largely contribute to the Fermi surface due to the weak spin orbit coupling. Because of this, even if the zone-boundary DLN becomes flat, its location is away from the Fermi level, which weakens the magnetic instability driven by DLN. This is also consistent with the fact that U_c for Sr_2RhO_4 is bigger than that for Sr_2IrO_4. On the other hand, in the case of Ba_2IrO_4, the system has an AFM ground state although there is no rotation distortion. In this case, one may expect that our theory based on the zone-boundary DLN cannot be applied since the space group of the system remains symmorphic. However, even in this case, one can still use the $\sqrt{2} \times \sqrt{2}$-type doubled unit cell to describe the magnetic instability since the property of the system is independent of the unit cell choice. In fact, according to the DFT+SOC calculations,

the zone-boundary Dirac line node is still present if the band structure is plotted by using the doubled unit cell as shown in Fig. 7(c). The U_c for Ba_2IrO_4 is found to be bigger than that for Sr_2IrO_4, which is consistent with the fact that Sr_2IrO_4 has a bigger rotation angle. If the rotation angle is artificially introduced, one can also observe the flattening of the zone-boundary DLN in Ba_2IrO_4 as shown below.

2. Sr_2IrO_4

Here we provide additional DFT calculations varying the rotation angle θ, which is obtained by changing the Ir-O bond length while fixing the in-plane lattice constant. The θ-dependent evolution of DFT band structure for a monolayer is demonstrated in Figs. 8(a)–8(e). During the evolution of θ, the bandwidth of the DLNs changes consistent with Figs. 3(h)–3(l) as well as the tight-binding calculations in the main text. The emergence of flat DLNs is found in Fig. 8(c). The θ-dependent evolution of DFT band structure for bulk Sr_2IrO_4 is demonstrated in Figs. 8(f)–8(j), which agrees with Figs. 3(m)–3(q) in the main text. The emergence of almost flat bands from the DFT calculations strongly supports the robustness of our theory on the tunability of DLN via rotation distortion of octahedra in layered perovskite oxides.

3. Sr_2RhO_4

Here we provide DFT calculations of Sr_2RhO_4 varying the rotation angle θ, which is obtained by changing the in-plane
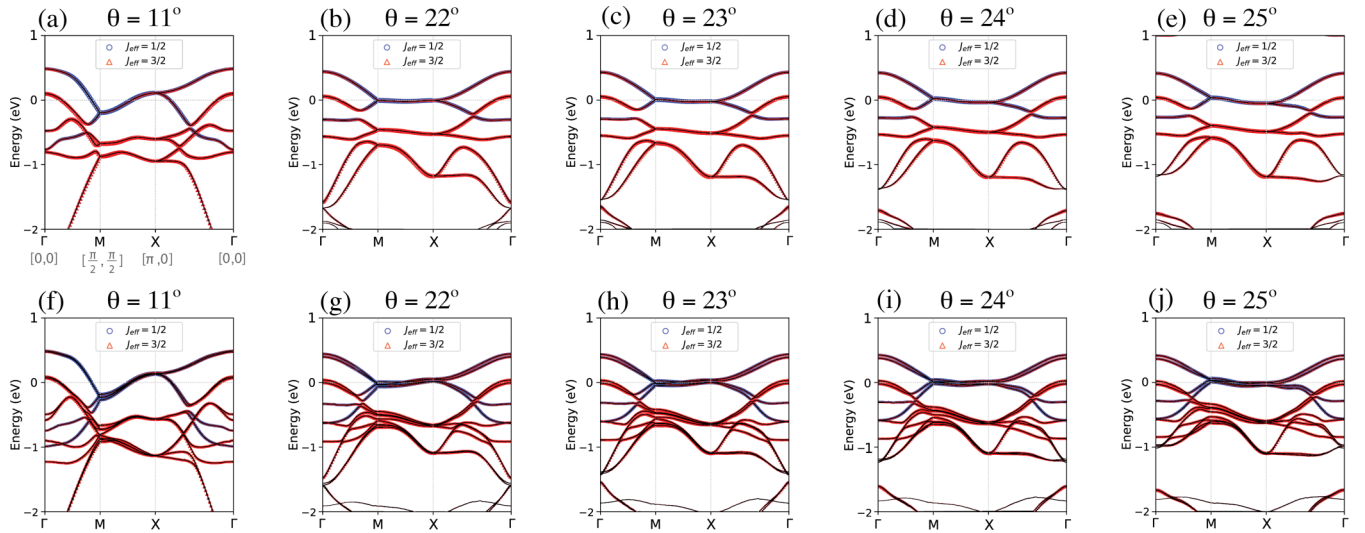
FIG. 8. (a)–(j) DFT band structures of Sr_2IrO_4 as a function of in-plane rotation angle θ, which is obtained by changing the Ir-O bond length while the in-plane lattice constant is fixed. (a)–(e) Band structure of a monolayer. (f)–(j) Band structure of the bulk. $J_{eff} = 1/2$ (blue circle) and $J_{eff} = 3/2$ (red triangle) bands are displayed by using different colors. The degenerate DLNs along the BZ boundary (M-X line) around the Fermi level become almost dispersionless at the critical angle $\theta \approx 23°$ in both a monolayer and the bulk Sr_2IrO_4 as shown in Figs. 8(c) and 8(h), respectively.

lattice constant while the Rh-O bond length is fixed as in Figs. 9(a)–9(c) (bulk) and 9(g)–9(i) (1ML), and by changing the Rh-O bond length while fixing the in-plane lattice constant in Figs. 9(d)–9(f) (bulk) and 9(j)–9(l) (1ML). The large contribution of $J_{eff} = 3/2$ states to the Fermi surface prevents Sr_2RhO_4 to fulfill the condition for half-filled $J_{eff} = 1/2$ states, but the θ-dependent evolution of DFT band structure is successfully demonstrated.
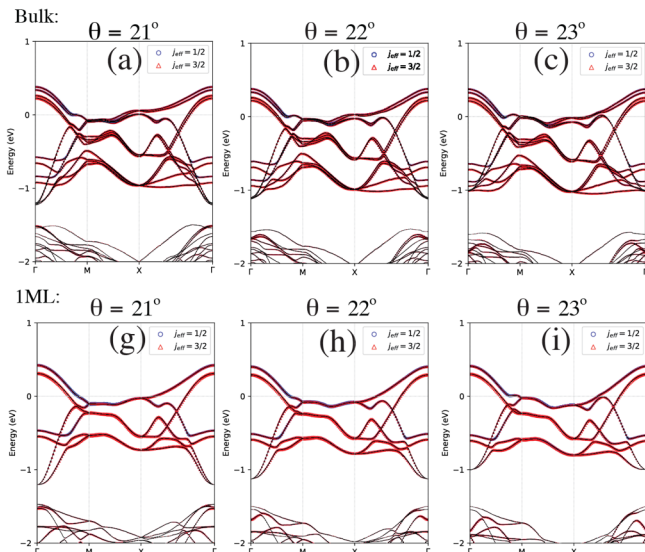
4. Ba$_2$IrO$_4$

Here we provide DFT band structure calculations of Ba_2IrO_4 varying the rotation angle θ, which is obtained by

changing the in-plane lattice constant while the Ir-O bond length is fixed as in Figs. 9(a)–9(c) (bulk) and 9(g)–9(i) (1ML), and by changing the Ir-O bond length while fixing the in-plane lattice constant in Figs. 9(d)–9(f) (bulk) and 9(j)–9(l) (1ML). One can find the almost flat band along the BZ boundary for 1ML of $\theta = 16°$ as shown in Fig. 10(j).

APPENDIX D: DFT BAND STRUCTURE CALCULATIONS INCLUDING STAGGERED TETRAGONAL DISTORTION

The second harmonic generation measurement indicates that Sr_2IrO_4 has a $I4_1/a$ space group, which is also supported by neutron diffraction studies. In particular, the neu-
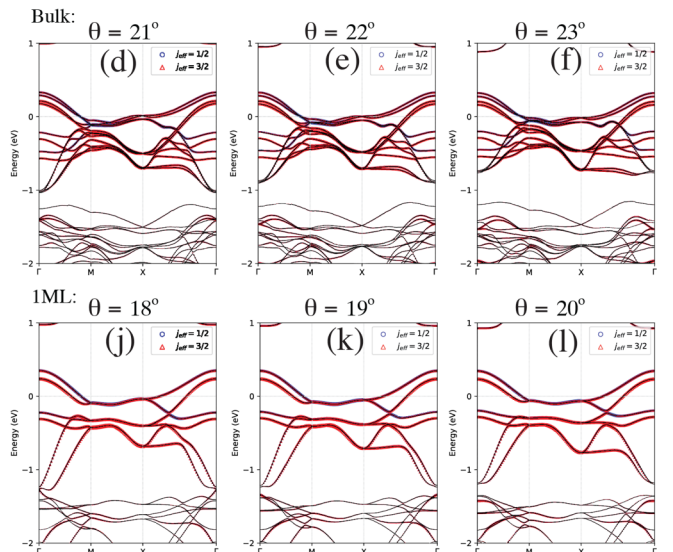

FIG. 9. The evolution of the Sr_2RhO_4 band structure obtained by DFT calculations varying the rotation angle θ. Here we implement two different ways of modifying the rotation angle both for bulk (a)–(f) and for 1ML (g)–(l).
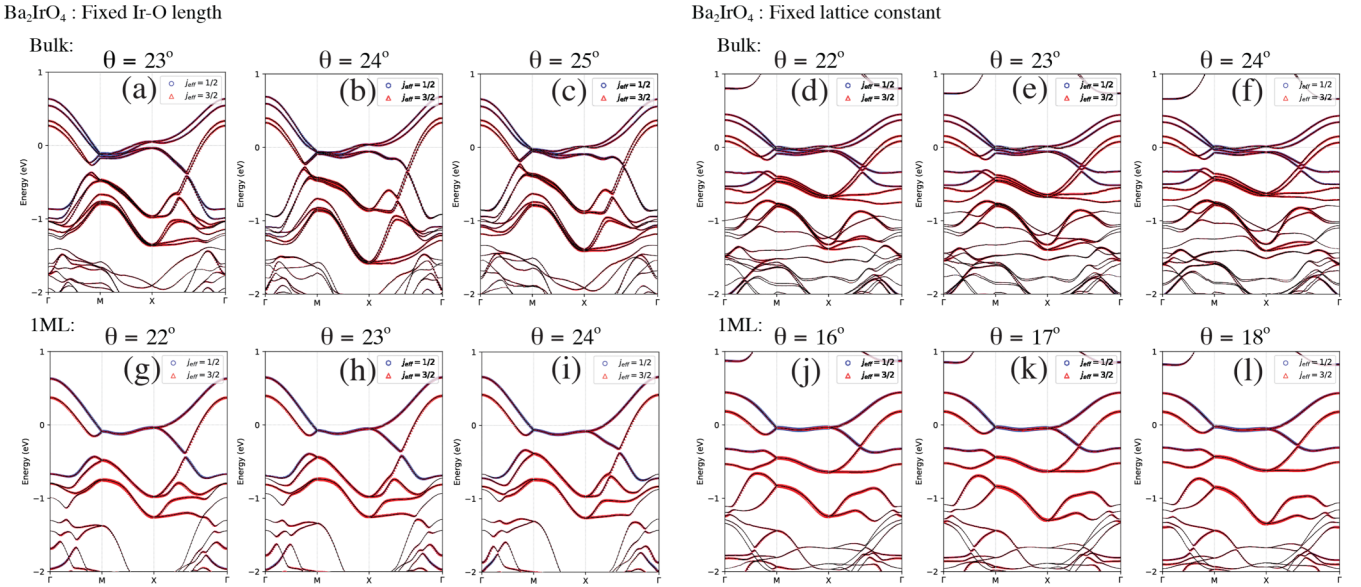
Ba$_2$IrO$_4$: Fixed Ir-O length

Bulk:

Ba$_2$IrO$_4$: Fixed lattice constant

Bulk:

FIG. 10. The evolution of the Ba$_2$IrO$_4$ band structure obtained by DFT calculations varying the rotation angle θ. Here we implement two different ways of modifying the rotation angle both for bulk (a)–(f) and for 1ML (g)–(l).

tron diffraction data reported in Ref. [9] identified the staggered pattern for tetragonal distortion of oxygen octahedron. Namely, in both A and B sublattices, the oxygen octahedron is elongated along the c direction, but the c/a ratios in A and B sublattices are slightly different. Here c/a ratio indicates the ratio of the out-of-plane Ir-O bond length over the in-plane Ir-O bond length. Such a staggered distortion of oxygen octahedron breaks the two glide mirror symmetries, which may affect the stability of the zone-boundary Dirac line node.

However, if we compare the actual Ir-O bond lengths at the two Ir sublattice sites (Ir$_1$ and Ir$_2$), one can expect that the staggered tetragonal distortion has a very tiny effect on the electronic properties. More explicitly, according to the neutron diffraction data shown in Table I of Ref. [9], the out-of-plane and in-plane Ir-O distance in the unit of angstrom are given by (2.056, 1.981) for Ir$_1$ and (2.057, 1.979) for Ir$_2$. The corresponding c/a ratios are $c/a = 1.038$ for Ir$_1$ and $c/a = 1.039$ for Ir$_2$, respectively. Namely, the relative change of Ir-O bond distances for two iridium sites is on the order of 10^{-3}, which is sufficient to produce a superlattice peak for structure analysis but is too tiny to affect the bulk electronic properties.

To demonstrate the negligible influence of the staggered tetragonal distortion on the electronic band structure, we performed additional DFT+SOC calculations taking into account the staggered tetragonal distortion in Fig. 11. When $c/a = $ (1.038, 1.039) in two sublattices, which is the experimental value, one can see that staggered distortion indeed has a negligible effect on the band degeneracy of the zone-boundary Dirac line node (on the MX line) as shown in Fig. 11(a). Only when the staggering of the c/a ratio is increased artificially up to $c/a = $ (1.030, 1047) shown in Fig. 11(d), the weak splitting of the band degeneracy along the MX direction can be observed. This clearly shows that the influence of the staggered tetragonal distortion on the electronic band structure is negligible and thus our theory of 2D Peierls instability can be applied to Sr$_2$IrO$_4$.

APPENDIX E: SUSCEPTIBILITY WITH SUBLATTICE, SPIN, AND LAYER DEGREES OF FREEDOM

The general form of susceptibility depends on the sublattice, spin, and layer indices:

$$\chi^{ij}_{\alpha\alpha',ll'}(\mathbf{q}) = -\int_0^\beta d\tau \langle S^i_{\alpha l}(\mathbf{q},\tau) S^j_{\alpha'l'}(-\mathbf{q},0)\rangle, \quad \text{(E1)}$$

where α, α' and l, l' indicate the sublattice and layer indices, respectively. The relevant physical susceptibility can be expressed as

$$\chi^{zz}_{\text{AFM}}(\mathbf{q}, i\nu_n) = \frac{1}{\beta V}\sum_{\mathbf{k}}\sum_{i\omega}\text{Tr}[G(\mathbf{k}, i\omega_n)(\tau^z\sigma^z\rho^z\eta^z)$$
$$\times G(\mathbf{k}+\mathbf{q}, i\omega_n+i\nu_n)(\tau^z\sigma^z\rho^z\eta^z)],$$

$$\chi^{zz}_{\text{FM}}(\mathbf{q}, i\nu_n) = \frac{1}{\beta V}\sum_{\mathbf{k}}\sum_{i\omega}\text{Tr}[G(\mathbf{k}, i\omega_n)(\tau^0\sigma^z\rho^z\eta^z)$$
$$\times G(\mathbf{k}+\mathbf{q}, i\omega_n+i\nu_n)(\tau^0\sigma^z\rho^z\eta^z)],$$

$$\chi^{+-}_{\text{AFM}}(\mathbf{q}, i\nu_n) = \frac{1}{\beta V}\sum_{\mathbf{k}}\sum_{i\omega}\text{Tr}[G(\mathbf{k}, i\omega_n)(\tau^z(\sigma^x+i\sigma^y)\rho^z\eta^z)$$
$$\times G(\mathbf{k}+\mathbf{q}, i\omega_n+i\nu_n)(\tau^z(\sigma^x-i\sigma^y)\rho^z\eta^z)],$$

$$\chi^{+-}_{\text{FM}}(\mathbf{q}, i\nu_n) = \frac{1}{\beta V}\sum_{\mathbf{k}}\sum_{i\omega}\text{Tr}[G(\mathbf{k}, i\omega_n)(\tau^0(\sigma^x+i\sigma^y)\rho^z\eta^z)$$
$$\times G(\mathbf{k}+\mathbf{q}, i\omega_n+i\nu_n)(\tau^0(\sigma^x-i\sigma^y)\rho^z\eta^z)].$$
$$\text{(E2)}$$

With antiferromagnetic interlayer coupling fixed to $\rho^z\eta^z = \begin{pmatrix} 1 & 0 & 0 & 0 \\ 0 & -1 & 0 & 0 \\ 0 & 0 & -1 & 0 \\ 0 & 0 & 0 & 1 \end{pmatrix}$ in a manner of the up-down-down-up spin configuration, we focus on spin susceptibility in 2D. In that sense, the four susceptibilities of χ^{zz}_{AFM}, χ^{zz}_{FM}, χ^{+-}_{AFM}, χ^{+-}_{FM} are
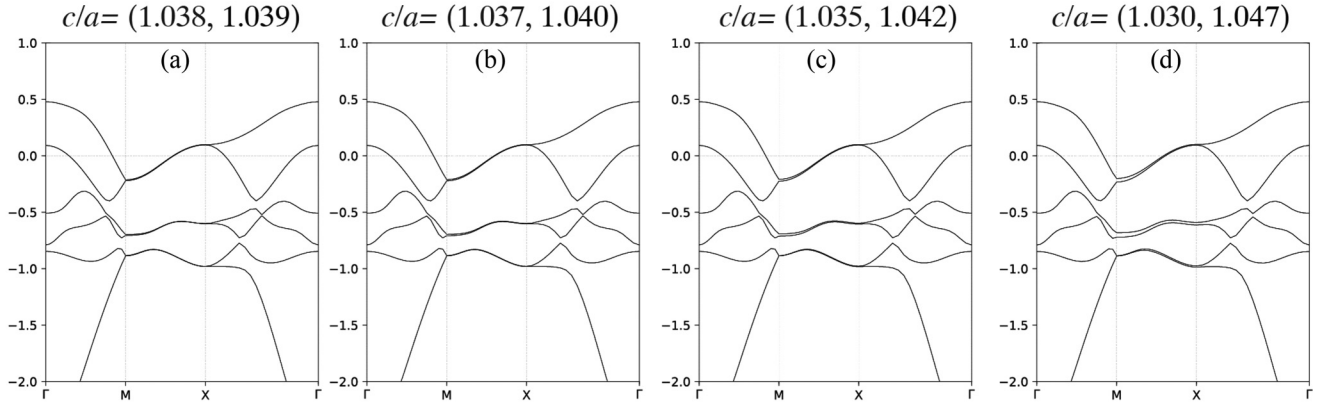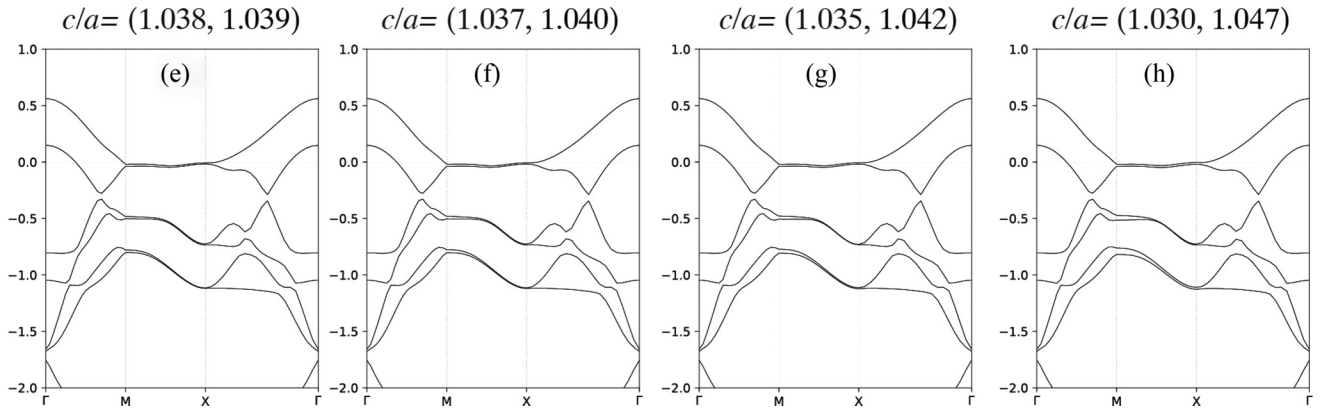
Staggered c/a with $11°$ rotation

Staggered c/a with $23°$ rotation

FIG. 11. DFT+SOC calculations of Sr_2IrO_4 monolayer with staggered tetragonal distortions. (a)–(d) The band structure obtained by varying c/a ratios with $\theta = 11°$. The energy splitting due to the staggered tetragonal distortion is negligible in the energy scale of Dirac line node dispersion. (e)–(h) The band structure obtained by varying c/a ratios with $\theta = 23°$ when the zone-boundary DLN is flat. The energy splitting due to the staggered tetragonal distortion is negligible.

taken into account. Further evaluation of Eq. (E2) reads

$$\text{Tr}[\cdots]_{\text{AFM}}^{zz} = 16\big((i\omega_n - \varepsilon_{\mathbf{k}}^0)(i\omega_n + i\nu_n - \varepsilon_{\mathbf{k+q}}^0) + \Delta_{\mathbf{k,q}}^1\big)$$
$$\times (N_{\mathbf{k}}(i\omega_n)N_{\mathbf{k+q}}(i\omega_n + i\nu_n))^{-1},$$

$$\text{Tr}[\cdots]_{\text{FM}}^{zz} = 16\big((i\omega_n - \varepsilon_{\mathbf{k}}^0)(i\omega_n + i\nu_n - \varepsilon_{\mathbf{k+q}}^0) + \Delta_{\mathbf{k,q}}^2\big)$$
$$\times (N_{\mathbf{k}}(i\omega_n)N_{\mathbf{k+q}}(i\omega_n + i\nu_n))^{-1},$$

$$\text{Tr}[\cdots]_{\text{AFM}}^{+-} = 32\big((i\omega_n - \varepsilon_{\mathbf{k}}^0)(i\omega_n + i\nu_n - \varepsilon_{\mathbf{k+q}}^0) + \Delta_{\mathbf{k,q}}^3\big)$$
$$\times (N_{\mathbf{k}}(i\omega_n)N_{\mathbf{k+q}}(i\omega_n + i\nu_n))^{-1},$$

$$\text{Tr}[\cdots]_{\text{FM}}^{+-} = 32\big((i\omega_n - \varepsilon_{\mathbf{k}}^0)(i\omega_n + i\nu_n - \varepsilon_{\mathbf{k+q}}^0) + \Delta_{\mathbf{k,q}}^4\big)$$
$$\times (N_{\mathbf{k}}(i\omega_n)N_{\mathbf{k+q}}(i\omega_n + i\nu_n))^{-1}, \quad (\text{E3})$$

where we have

$$\Delta_{\mathbf{k,q}}^1 = -\varepsilon_{\mathbf{k}}^{ad}\varepsilon_{\mathbf{k+q}}^{ad} - \varepsilon_{\mathbf{k}}^{ad'}\varepsilon_{\mathbf{k+q}}^{ad'} - \varepsilon_{\mathbf{k}}^{b}\varepsilon_{\mathbf{k+q}}^{b} + \varepsilon_{\mathbf{k}}^{bd}\varepsilon_{\mathbf{k+q}}^{bd}$$
$$+ \varepsilon_{\mathbf{k}}^{bx}\varepsilon_{\mathbf{k+q}}^{bx} + \varepsilon_{\mathbf{k}}^{by}\varepsilon_{\mathbf{k+q}}^{by} + \varepsilon_{\mathbf{k}}^{bz}\varepsilon_{\mathbf{k+q}}^{bz} + \varepsilon_{\mathbf{k}}^{c}\varepsilon_{\mathbf{k+q}}^{c}$$

$$- \varepsilon_{\mathbf{k}}^{cd}\varepsilon_{\mathbf{k+q}}^{cd} + \varepsilon_{\mathbf{k}}^{cx}\varepsilon_{\mathbf{k+q}}^{cx} + \varepsilon_{\mathbf{k}}^{cy}\varepsilon_{\mathbf{k+q}}^{cy} - \varepsilon_{\mathbf{k}}^{cz}\varepsilon_{\mathbf{k+q}}^{cz},$$

$$\Delta_{\mathbf{k,q}}^2 = \varepsilon_{\mathbf{k}}^{ad}\varepsilon_{\mathbf{k+q}}^{ad} + \varepsilon_{\mathbf{k}}^{ad'}\varepsilon_{\mathbf{k+q}}^{ad'} - \varepsilon_{\mathbf{k}}^{b}\varepsilon_{\mathbf{k+q}}^{b} - \varepsilon_{\mathbf{k}}^{bd}\varepsilon_{\mathbf{k+q}}^{bd}$$
$$- \varepsilon_{\mathbf{k}}^{bx}\varepsilon_{\mathbf{k+q}}^{bx} - \varepsilon_{\mathbf{k}}^{by}\varepsilon_{\mathbf{k+q}}^{by} - \varepsilon_{\mathbf{k}}^{bz}\varepsilon_{\mathbf{k+q}}^{bz} + \varepsilon_{\mathbf{k}}^{c}\varepsilon_{\mathbf{k+q}}^{c}$$
$$+ \varepsilon_{\mathbf{k}}^{cd}\varepsilon_{\mathbf{k+q}}^{cd} - \varepsilon_{\mathbf{k}}^{cx}\varepsilon_{\mathbf{k+q}}^{cx} - \varepsilon_{\mathbf{k}}^{cy}\varepsilon_{\mathbf{k+q}}^{cy} + \varepsilon_{\mathbf{k}}^{cz}\varepsilon_{\mathbf{k+q}}^{cz},$$

$$\Delta_{\mathbf{k,q}}^3 = -\varepsilon_{\mathbf{k}}^{ad}\varepsilon_{\mathbf{k+q}}^{ad} + \varepsilon_{\mathbf{k}}^{ad'}\varepsilon_{\mathbf{k+q}}^{ad'} - \varepsilon_{\mathbf{k}}^{b}\varepsilon_{\mathbf{k+q}}^{b} + \varepsilon_{\mathbf{k}}^{bd}\varepsilon_{\mathbf{k+q}}^{bd}$$
$$- \varepsilon_{\mathbf{k}}^{bz}\varepsilon_{\mathbf{k+q}}^{bz} + \varepsilon_{\mathbf{k}}^{c}\varepsilon_{\mathbf{k+q}}^{c} - \varepsilon_{\mathbf{k}}^{cd}\varepsilon_{\mathbf{k+q}}^{cd} + \varepsilon_{\mathbf{k}}^{cz}\varepsilon_{\mathbf{k+q}}^{cz},$$

$$\Delta_{\mathbf{k,q}}^4 = \varepsilon_{\mathbf{k}}^{ad}\varepsilon_{\mathbf{k+q}}^{ad} - \varepsilon_{\mathbf{k}}^{ad'}\varepsilon_{\mathbf{k+q}}^{ad'} - \varepsilon_{\mathbf{k}}^{b}\varepsilon_{\mathbf{k+q}}^{b} - \varepsilon_{\mathbf{k}}^{bd}\varepsilon_{\mathbf{k+q}}^{bd}$$
$$+ \varepsilon_{\mathbf{k}}^{bz}\varepsilon_{\mathbf{k+q}}^{bz} + \varepsilon_{\mathbf{k}}^{c}\varepsilon_{\mathbf{k+q}}^{c} + \varepsilon_{\mathbf{k}}^{cd}\varepsilon_{\mathbf{k+q}}^{cd} - \varepsilon_{\mathbf{k}}^{cz}\varepsilon_{\mathbf{k+q}}^{cz},$$

$$N_{\mathbf{k}}(i\omega_n) = (i\omega_n - \varepsilon_{\mathbf{k}}^0)^2 - (\varepsilon_{\mathbf{k}}^{ad})^2 - (\varepsilon_{\mathbf{k}}^{ad'})^2 - (\varepsilon_{\mathbf{k}}^{b})^2$$
$$- (\varepsilon_{\mathbf{k}}^{bd})^2 - (\varepsilon_{\mathbf{k}}^{bx})^2 - (\varepsilon_{\mathbf{k}}^{by})^2 - (\varepsilon_{\mathbf{k}}^{bz})^2$$
$$- (\varepsilon_{\mathbf{k}}^{c})^2 - (\varepsilon_{\mathbf{k}}^{cd})^2 - (\varepsilon_{\mathbf{k}}^{cx})^2 - (\varepsilon_{\mathbf{k}}^{cy})^2 - (\varepsilon_{\mathbf{k}}^{cz})^2$$
$$= \big((i\omega_n - \varepsilon_{\mathbf{k}}^0) + Z_{\mathbf{k}}\big)\big((i\omega_n - \varepsilon_{\mathbf{k}}^0) - Z_{\mathbf{k}}\big), \quad (\text{E4})$$

with

$$Z_{\mathbf{k}} = \left[\left(\varepsilon_{\mathbf{k}}^{ad}\right)^2 + \left(\varepsilon_{\mathbf{k}}^{ad'}\right)^2 + \left(\varepsilon_{\mathbf{k}}^{b}\right)^2 + \left(\varepsilon_{\mathbf{k}}^{bd}\right)^2 + \left(\varepsilon_{\mathbf{k}}^{bx}\right)^2 \right.$$
$$+ \left(\varepsilon_{\mathbf{k}}^{by}\right)^2 + \left(\varepsilon_{\mathbf{k}}^{bz}\right)^2 + \left(\varepsilon_{\mathbf{k}}^{c}\right)^2 + \left(\varepsilon_{\mathbf{k}}^{cd}\right)^2 + \left(\varepsilon_{\mathbf{k}}^{cx}\right)^2$$
$$+ \left. \left(\varepsilon_{\mathbf{k}}^{cy}\right)^2 + \left(\varepsilon_{\mathbf{k}}^{cz}\right)^2 \right]^{1/2}. \tag{E5}$$

The replacement $\mathbf{k} \to \mathbf{k} + \mathbf{q}$ and $i\omega_n \to i\omega_n + i\nu_n$ in Eqs. (E4) and (E5) can yield $N_{\mathbf{k}+\mathbf{q}}(i\omega_n + i\nu_n)$ and $Z_{\mathbf{k}+\mathbf{q}}$.

After Matsubara summation, we arrive at

$$\chi_{\text{AFM}}^{zz}(\mathbf{q}, i\nu_n) = \frac{1}{V}\sum_{\mathbf{k}}\left[\frac{1}{Z_{\mathbf{k}}^2 - Z_{\mathbf{k}+\mathbf{q}}^4}\left(4 + \frac{4\Delta_{\mathbf{k},\mathbf{q}}^1}{Z_{\mathbf{k}} Z_{\mathbf{k}+\mathbf{q}}}\right)\right.$$
$$\times \left(\frac{1}{e^{\beta Z_{\mathbf{k}}^2}+1} - \frac{1}{e^{\beta Z_{\mathbf{k}+\mathbf{q}}^4}+1}\right)$$
$$+ \frac{1}{Z_{\mathbf{k}}^1 - Z_{\mathbf{k}+\mathbf{q}}^3}\left(4 + \frac{4\Delta_{\mathbf{k},\mathbf{q}}^1}{Z_{\mathbf{k}} Z_{\mathbf{k}+\mathbf{q}}}\right)\left(\frac{1}{e^{\beta Z_{\mathbf{k}}^1}+1} - \frac{1}{e^{\beta Z_{\mathbf{k}+\mathbf{q}}^3}+1}\right)$$
$$+ \frac{1}{Z_{\mathbf{k}}^2 - Z_{\mathbf{k}+\mathbf{q}}^3}\left(4 - \frac{4\Delta_{\mathbf{k},\mathbf{q}}^1}{Z_{\mathbf{k}} Z_{\mathbf{k}+\mathbf{q}}}\right)\left(\frac{1}{e^{\beta Z_{\mathbf{k}}^2}+1} - \frac{1}{e^{\beta Z_{\mathbf{k}+\mathbf{q}}^3}+1}\right)$$
$$+ \left. \frac{1}{Z_{\mathbf{k}}^1 - Z_{\mathbf{k}+\mathbf{q}}^4}\left(4 - \frac{4\Delta_{\mathbf{k},\mathbf{q}}^1}{Z_{\mathbf{k}} Z_{\mathbf{k}+\mathbf{q}}}\right)\left(\frac{1}{e^{\beta Z_{\mathbf{k}}^1}+1} - \frac{1}{e^{\beta Z_{\mathbf{k}+\mathbf{q}}^4}+1}\right)\right]. \tag{E6}$$

The replacement of n in $\Delta_{\mathbf{k},\mathbf{q}}^n$ with $n = 1, 2, 3, 4$ and the proper choice of constant factors of 4 or 8 can give us all kinds of physical spin susceptibility defined in Eq. (E2).

1. RPA calculation with sublattice degree of freedom

In this section, we present results for the magnetic nesting instabilities within the tight-binding random phase approximation (RPA) model including the sublattice and $J_{\text{eff}} = 1/2$ degree of freedoms. We thus provide the sign and factor in front of U for the RPA calculation of the spin susceptibility. With the final result in Eq. (E14) below, we can determine the critical value of U when the denominator satisfies the divergence condition, for example, $1 = U\chi_0(\mathbf{q})$ with the perfect nesting vector $\mathbf{q}$. The obtained critical values of U as a function of the rotational angle θ enable us to determine the phase boundary of the magnetic phase diagram in the main text. Let us first write down spin susceptibility in the AB-sublattice system.

$$\chi_{AB}^{+-}(\mathbf{q}, \tau) = -\frac{1}{V}\sum_{\mathbf{p},\mathbf{k}}\sum_{\sigma_1,\sigma_1'}\sum_{\sigma_2,\sigma_2'}\sum_{\alpha_1,\alpha_1'}\sum_{\beta_1,\beta_1'}\langle \mathbb{T}_\tau C_{\mathbf{k},\alpha_1,\sigma_1}^\dagger(\tau)$$
$$\times (\sigma^+)_{\sigma_1,\sigma_1'}(s^z)_{\alpha_1,\alpha_1'} C_{\mathbf{k}+\mathbf{q},\alpha_1',\sigma_1'}(\tau)$$
$$\times C_{\mathbf{p}+\mathbf{q},\beta_1,\sigma_2}^\dagger(0)(\sigma^-)_{\sigma_2,\sigma_2'}(s^z)_{\beta_1,\beta_1'} C_{\mathbf{p},\beta_1',\sigma_2'}(0)\rangle$$
$$= \frac{1}{V}\sum_{\mathbf{p},\mathbf{k}}\sum_{\sigma_1,\sigma_1'}\sum_{\sigma_2,\sigma_2'}\sum_{\alpha_1,\alpha_1'}\sum_{\beta_1,\beta_1'}(\sigma^+)_{\sigma_1,\sigma_1'}(s^z)_{\alpha_1,\alpha_1'}$$
$$\times (\sigma^-)_{\sigma_2,\sigma_2'}(s^z)_{\beta_1,\beta_1'}\langle \mathbb{T}_\tau C_{\mathbf{p},\beta_1',\sigma_2'}(0)$$
$$\times C_{\mathbf{k}\alpha_1,\sigma_1}^\dagger(\tau) C_{\mathbf{k}+\mathbf{q},\alpha_1',\sigma_1'}(\tau) C_{\mathbf{p}+\mathbf{q},\beta_1,\sigma_2}^\dagger(0)\rangle, \tag{E7}$$

where $\alpha_1, \alpha_1', \beta_1, \beta_1'$ denote the sublattice indices and $\sigma_1, \sigma_1', \sigma_2, \sigma_2'$ the spin indices. Here τ serves as the imaginary

time not sublattice index as in the main text. We formulate the equation of motion for RPA susceptibility. The derivatives of $\Theta(\tau)$ function in the bracket gives $\delta(\tau)$ function

$$\delta(0)\langle C_{\mathbf{p},\beta_1',\sigma_2'}(0) C_{\mathbf{k},\alpha_1,\sigma_1}^\dagger(0) C_{\mathbf{k}+\mathbf{q},\alpha_1',\sigma_1'}(0) C_{\mathbf{p}+\mathbf{q},\beta_1,\sigma_2}^\dagger(0)\rangle$$
$$= -\langle C_{\mathbf{k},\alpha_1,\sigma_1}^\dagger C_{\mathbf{k}+\mathbf{q},\alpha_1',\sigma_1'} C_{\mathbf{p}+\mathbf{q},\beta_1,\sigma_2}^\dagger C_{\mathbf{p},\beta_1',\sigma_2'}\rangle. \tag{E8}$$

Employing Wick's theorem, Eq. (E8) becomes

$$- \langle C_{\mathbf{k},\alpha_1,\sigma_1}^\dagger C_{\mathbf{k}+\mathbf{q},\alpha_1',\sigma_1'}\rangle\langle C_{\mathbf{p}+\mathbf{q},\beta_1,\sigma_2}^\dagger C_{\mathbf{p},\beta_1',\sigma_2'}\rangle$$
$$- \langle C_{\mathbf{k},\alpha_1,\sigma_1}^\dagger C_{\mathbf{p},\beta_1',\sigma_2'}\rangle\langle C_{\mathbf{p}+\mathbf{q},\beta_1,\sigma_2}^\dagger C_{\mathbf{k}+\mathbf{q},\alpha_1',\sigma_1'}\rangle$$
$$+ \langle C_{\mathbf{k},\alpha_1,\sigma_1}^\dagger C_{\mathbf{p}+\mathbf{q},\beta_1,\sigma_2}^\dagger\rangle\langle C_{\mathbf{k}+\mathbf{q},\alpha_1',\sigma_1'} C_{\mathbf{p},\beta_1',\sigma_2'}\rangle$$
$$= -\langle C_{\mathbf{k},\alpha_1,\sigma_1}^\dagger C_{\mathbf{p},\beta_1',\sigma_2'}\rangle\delta_{\mathbf{p},\mathbf{k}}\delta_{\beta_1,\alpha_1'}\delta_{\sigma_2,\sigma_1'}$$
$$+ \langle C_{\mathbf{p}+\mathbf{q},\beta_1,\sigma_2}^\dagger C_{\mathbf{k}+\mathbf{q},\alpha_1',\sigma_1'}\rangle\delta_{\mathbf{p},\mathbf{k}}\delta_{\beta_1',\alpha_1}\delta_{\sigma_2',\sigma_1}, \tag{E9}$$

where only the second term in the first line contributes to the last line accounting for the matrix element of σ^+ and σ^- and $\langle C^\dagger C^\dagger\rangle = \langle CC\rangle = 0$. Implementing σ^+, σ^-, and s^z, Eq. (E9) reads

$$- \langle C_{\mathbf{k},\alpha_1,\sigma_1}^\dagger C_{\mathbf{p},\beta_1',\sigma_2'}\rangle(\sigma^+)_{\sigma_1\sigma_1'}(\sigma^-)_{\sigma_1'\sigma_2'}(s^z)_{\alpha_1\alpha_1'}(s^z)_{\alpha_1'\beta_1'}$$
$$+ \langle C_{\mathbf{p}+\mathbf{q},\beta_1,\sigma_2}^\dagger C_{\mathbf{k}+\mathbf{q},\alpha_1',\sigma_1'}\rangle(\sigma^+)_{\sigma_1\sigma_1'}(\sigma^-)_{\sigma_2\sigma_1}(s^z)_{\alpha_1\alpha_1'}(s^z)_{\beta_1\alpha_1}$$
$$= -\langle n_{\mathbf{k},\alpha,\uparrow}\rangle + \langle n_{\mathbf{k}+\mathbf{q},\alpha,\downarrow}\rangle, \tag{E10}$$

where we reach the last line when the spin index summations are applied. Next, we should evaluate the $\frac{\partial}{\partial\tau}C_{\mathbf{k},\alpha,\sigma}^\dagger(\tau)$. The Hamiltonian is given by

$$H = H_0 + H_{\text{int}} = \sum_{\mathbf{k}',\alpha,\sigma}\varepsilon_{\mathbf{k}'}C_{\mathbf{k}',\alpha,\sigma}^\dagger C_{\mathbf{k}',\alpha,\sigma}$$
$$+ \frac{U}{N}\sum_{\mathbf{p},\mathbf{l},\mathbf{q}_1,\sigma,\sigma',b} C_{\mathbf{p},b,\sigma}^\dagger C_{\mathbf{l},b,\sigma'}^\dagger C_{\mathbf{l}+\mathbf{q}_1,b,\sigma'} C_{\mathbf{p}-\mathbf{q}_1,b,\sigma}, \tag{E11}$$

with b the sublattice index. There is no intersublattice mixing term in the Hubbard interaction due to the nature of on-site interaction. We obtain

$$[H_0, C_{\mathbf{k},\alpha_1,\sigma_1}^\dagger](\tau) = \varepsilon_{\mathbf{k}} C_{\mathbf{k},\alpha_1,\sigma_1}^\dagger(\tau),$$
$$[H_0, C_{\mathbf{k}+\mathbf{q},\alpha_1',\sigma_1'}](\tau) = -\varepsilon_{\mathbf{k}+\mathbf{q}} C_{\mathbf{k}+\mathbf{q},\alpha_1',\sigma_1'}(\tau),$$
$$[H_{\text{int}}, C_{\mathbf{k},\alpha_1,\sigma_1}^\dagger](\tau)$$
$$= \frac{U}{N}\sum_{\mathbf{p},\mathbf{l},\mathbf{q}_1,\sigma,\sigma',b}\left(C_{\mathbf{k}+\mathbf{q}_1,\alpha_1,\sigma_1}^\dagger C_{\mathbf{l},\alpha_1,\sigma'}^\dagger C_{\mathbf{l}+\mathbf{q}_1,\alpha_1,\sigma'}\right.$$
$$\left. - C_{\mathbf{p},\alpha_1,\sigma}^\dagger C_{\mathbf{k}-\mathbf{q}_1,\alpha_1,\sigma_1}^\dagger C_{\mathbf{p}-\mathbf{q}_1,\alpha_1,\sigma}\right)(\tau),$$
$$[H_{\text{int}}, C_{\mathbf{k}+\mathbf{q},\alpha_1',\sigma_1'}](\tau)$$
$$= \frac{U}{N}\sum\left(C_{\mathbf{p},\alpha_1',\sigma}^\dagger C_{\mathbf{k}+\mathbf{q}+\mathbf{q}_1,\alpha_1',\sigma_1'} C_{\mathbf{p}-\mathbf{q}_1,\alpha_1',\sigma}\right.$$
$$\left. C_{\mathbf{l},\alpha_1',\sigma'}^\dagger C_{\mathbf{l}+\mathbf{q}_1,\alpha_1',\sigma'} C_{\mathbf{k}+\mathbf{q}-\mathbf{q}_1,\alpha_1',\sigma_1'}\right)(\tau). \tag{E12}$$

The third and fourth commutators gives $-\langle n_{\mathbf{k},\alpha_1,\uparrow}\rangle$ and $\langle n_{\mathbf{k}+\mathbf{q},\alpha_1',\downarrow}\rangle$ contributions. The resultant Dyson's equation is thus

$$(i\omega_n - \varepsilon_{\mathbf{k}} + \varepsilon_{\mathbf{k}+\mathbf{k}})\chi_{AB}^{+-}(\mathbf{q}, i\omega_n)$$
$$= (-\langle n_{\mathbf{k},\alpha_1,\uparrow}\rangle + \langle n_{\mathbf{k}+\mathbf{q},\alpha_1',\downarrow}\rangle)(1 + U\chi_{AB}^{+-}(\mathbf{q}, i\omega_n)). \tag{E13}$$

So, we have

$$\chi_{AB}^{+-}(\mathbf{q}, i\omega_n) = \frac{(\chi_{AB}^{+-}(\mathbf{q}, i\omega_n))_0}{1 - U(\chi_{AB}^{+-}(\mathbf{q}, i\omega_n))_0}. \tag{E14}$$

2. Tetrahedron methods in the two-dimensional system

As noted in Eq. (E6), the spin susceptibility takes the following form

$$\chi_{nn'}(\mathbf{q}) = \frac{1}{V} \sum_{\mathbf{k}} \frac{1}{E_n(\mathbf{k}) - E_{n'}(\mathbf{k} + \mathbf{q})}. \tag{E15}$$

The susceptibility diverges when it satisfies the nesting condition $E_n(\mathbf{k}) = E_{n'}(\mathbf{k} + \mathbf{q})$. Here we provide the analytic expression for $\chi_{nn'}(\mathbf{q})$ by using the tetrahedron methods. In the previous work by Rath and Freeman in 1975 [41], the tetrahedron methods are subjected to the integral over the three-dimensional $\mathbf{k}$ space. A variant formula to two-dimensional $\mathbf{k}$ space seems obvious, but it is worth clarifying explicit form. Let us choose the coordinates of the corners of triangle

$$\mathbf{k}_1 = (0, 0), \ \mathbf{k}_2 = (X_1, 0), \ \mathbf{k}_2 = (X_2, Y_2), \tag{E16}$$

and we define $V_i = E_{n'}(\mathbf{k}_i + \mathbf{q}) - E_n(\mathbf{k}_i)$ where $i = 1, 2, 3$. We then expand the energy difference linearly

$$E_{n'}(\mathbf{k} + \mathbf{q}) - E_n(\mathbf{k}) = A + Bx + Cy. \tag{E17}$$

Here the coefficients A, B, C can be obtained from the energy difference at the corner of the triangle:

$$A = V_1, \ A + BX_1 = V_2, \ A + BX_2 + CY_2 = V_3. \tag{E18}$$

The integral over the triangle can be written as

$$\chi = \int_0^{Y_2} dy \left[\int_{\frac{X_2}{Y_2}y}^{\frac{(X_2-X_1)}{Y_2}y+X_1} \frac{1}{A + Bx + Cy} \right]. \tag{E19}$$

Basically, we assume $V_1 < V_2 < V_3$. For analytic expression, we have

$$\chi = \frac{V_1 \ln(|V_1|)}{(V_1 - V_2)(V_1 - V_3)} + \frac{V_2 \ln(|V_2|)}{(V_3 - V_2)(V_1 - V_2)} + \frac{V_3 \ln(|V_3|)}{(V_3 - V_2)(V_3 - V_1)}. \tag{E20}$$

It holds true both for $V_1, V_2, V_3 > 0$ and $V_1, V_2, V_3 < 0$.

We must carefully treat the above expression in the limit of several cases:

(i) $V_1 = V_2 = V_3, V_1 > 0$ or $V_1 < 0$

$$\chi = \frac{1}{2V_1}. \tag{E21}$$

(ii) $V_1 = V_2 = V_3 = 0$

$$\chi = 0. \tag{E22}$$

(iii) $V_1 = V_2 \neq V_3, \ V_1 \neq 0, \ V_3 \neq 0, \ V_1 > 0, V_3 > 0$ and $V_1 < 0, V_3 < 0$

$$\chi = \frac{V_1 - V_3 + V_3 \ln\left(\left|\frac{V_3}{V_1}\right|\right)}{(V_1 - V_3)^2}. \tag{E23}$$

(iv-1) $V_1 = V_2 \neq V_3, V_1 \neq 0, V_3 = 0, V_1 > 0, V_1 < 0$

$$\chi = \frac{1}{V_1}. \tag{E24}$$

(iv-2) $V_1 = V_2 \neq V_3, V_1 = V_2 = 0, V_3 \neq 0$

$$\chi = 0. \tag{E25}$$

(v) $V_1 \neq V_2 = V_3, \ V_1 \neq 0, \ V_3 \neq 0, \ V_1 > 0, V_3 > 0$ and $V_1 < 0, V_3 < 0$

$$\chi = \frac{-V_1 + V_3 + V_1 \ln\left(\left|\frac{V_1}{V_3}\right|\right)}{(V_1 - V_3)^2}. \tag{E26}$$

(vi-1) $V_1 \neq V_2 = V_3, V_1 = 0, V_3 \neq 0, V_3 > 0, V_3 < 0$

$$\chi = \frac{1}{V_3}. \tag{E27}$$

(vi-2) $V_1 \neq V_2 = V_3, V_1 \neq 0, V_2 = V_3 = 0$

$$\chi = 0. \tag{E28}$$

(vii) $V_1 = 0, V_2 \neq V_3, V_2, V_3 > 0$

$$\chi = \frac{\ln\left(\left|\frac{V_2}{V_3}\right|\right)}{V_2 - V_3}. \tag{E29}$$

(viii) $V_3 = 0, V_1 \neq V_2, V_1, V_2 < 0$

$$\chi = \frac{\ln\left(\left|\frac{V_1}{V_2}\right|\right)}{V_1 - V_2}. \tag{E30}$$

(ix) $V_2 = 0, V_1 \neq V_3, V_1 < 0, V_3 > 0$

$$\chi = \frac{\ln\left(\left|\frac{V_1}{V_3}\right|\right)}{V_1 - V_3}. \tag{E31}$$

With this exact form of susceptibility one can properly capture the logarithmically diverging feature as in Fig. 5(d) in the main text.

APPENDIX F: SELF-CONSISTENT MEAN-FIELD CALCULATIONS

The divergent susceptibility due to dispersionless DLN indicates that the metallic state has an instability to a gapped phase which breaks the crystal symmetry leading to the AFM state. The specific ordering pattern suggested by the susceptibility calculation is the *ab*-plane canted AFM rather than the *c*-axis collinear AFM as shown in Fig. 5(c). To verify the magnetic ground state, we have performed the numerical analysis by means of self-consistent mean-field calculations. We allow the order parameters to describe any type of magnetic ordering patterns, thus we set $\mathbf{m}^A = (m_x^A, m_y^A, m_z^A)$ for sublattice A and $\mathbf{m}^B = (m_x^B, m_y^B, m_z^B)$ for sublattice B within a monolayer. The other order parameters in the remaining three layers are chosen by assuming the well-known "up-down-down-up" ordering pattern for net ferromagnetic moments [7,25]. The chemical potential μ is determined iteratively to ensure the half-filling condition. The tolerance factor for the numerical iteration is fixed to 10^{-5} to ensure the convergence of the order parameters and chemical potential for given (θ, U) during several hundreds of iteration times. The resulting phase diagram is shown in Fig. 5(e). In the regime for the *ab*-plane canted AFM phase, due to the spin anisotropy originating from interlayer coupling, the arbitrary initial value including the *c*-axis AFM converges into the *ab*-plane canted AFM as a final solution. We also have confirmed that the total energy of the *ab*-plane canted AFM is lower than that of the *c*-axis

AFM. The critical interaction U_c from self-consistent calculation agrees well with that from RPA-corrected susceptibility calculations. Convergence to ordered phase is tricky near critical rotational angle θ_c within our mean-field calculation scheme. More sophisticated numerical calculation may be needed to elaborate the results near the critical rotational angle. However, the overall tendency of the critical interaction U_c as a function of the rotational angle θ is consistent with each other as shown in Fig. 5(e).

APPENDIX G: LOCALIZED LINE STATES

We have introduced the diagonal line states in Eq. (5) providing us the basic building blocks to formulate the localized wave functions in the square lattice. Here, we will show that appropriate linear combinations of such localized diagonal line states with positive (negative) slope correspond to the degenerate eigenstates along the BZ boundary satisfying $k_x + k_y = \pi$ ($k_x - k_y = \pi$). From the localized diagonal line states in Eq. (5), using the Fourier transformation $c_\sigma^\dagger(\mathbf{r}) = \frac{1}{\sqrt{4N^2}} \sum_{\mathbf{k}} e^{-i\mathbf{k}\cdot\mathbf{r}} c_{\mathbf{k},\sigma}^\dagger$ we find

$$|\Psi\rangle_{A,\sigma}^\alpha(\phi) = \frac{1}{\sqrt{N}} \sum_{m=1}^{N} e^{i2m\phi} |\Psi\rangle_{\ell_\alpha=2m,\sigma}^\alpha$$

$$= \frac{1}{\sqrt{N}} \sum_{m=1}^{N} \frac{1}{\sqrt{2N}} \sum_{\mathbf{r}\in\ell_\alpha=2m}$$

$$\times \frac{1}{2N} \sum_{\mathbf{k}} e^{i2m\phi}(-1)^{r_x} e^{-i\mathbf{k}\cdot\mathbf{r}} c_{\mathbf{k},\sigma}^\dagger |0\rangle, \quad \text{(G1)}$$

where $\mathbf{r} = (r_x, r_x + 2m - 1)$ [$\mathbf{r} = (r_x, -r_x + 2m - 1)$] for $\alpha = p$ ($\alpha = n$) with $r_x = 1, 2, ..., 2N$. For a diagonal line with positive slope, we obtain

$$|\Psi\rangle_{A,\sigma}^p(\phi) = \frac{\sqrt{2}}{(2N)^2} \sum_{\mathbf{k}} \sum_{m=1}^{N} \sum_{r_x=1}^{2N}$$

$$\times e^{i2m\phi}(-1)^{r_x} e^{-i\mathbf{k}\cdot(r_x, r_x+2m-1)} c_{\mathbf{k},\sigma}^\dagger |0\rangle,$$

$$= \frac{\sqrt{2}}{(2N)^2} \sum_{\mathbf{k}} \sum_{m=1}^{N} \sum_{r_x=1}^{2N}$$

$$\times e^{i[r_x(\pi-k_x-k_y)+2m(\phi-k_y)+k_y]} c_{\mathbf{k},\sigma}^\dagger |0\rangle, \quad \text{(G2)}$$

which, in the thermodynamic limit, becomes

$$|\Psi\rangle_{A,\sigma}^p(\phi) = \frac{1}{\sqrt{2}} \sum_{\mathbf{k}} \delta_{0,\pi-k_x-k_y} \delta_{0,\phi-k_y} e^{ik_y} c_{\mathbf{k},\sigma}^\dagger |0\rangle,$$

$$= \frac{1}{\sqrt{2}} e^{i\phi} c_{(k_x=\pi-\phi,k_y=\phi),\sigma}^\dagger |0\rangle. \quad \text{(G3)}$$

In this way, we obtain the Bloch state $|\Psi\rangle_{A,\sigma}^p(\phi)$ which is defined along the BZ boundary satisfying $k_x + k_y = \pi$. The same property holds for $|\Psi\rangle_{\tau,\sigma}^\alpha(\phi)$ by changing sublattice τ, pseudospin σ, and slope α indices with the wave number ϕ defined along the BZ boundary satisfying $k_x + k_y = \pi$ ($k_x - k_y = \pi$) when it comes to positive (negative) slope. Finally, the explicit form of the critical rotational angle from the condition $t_2 = 2t_3$ is given by

$$\theta_c = \frac{1}{2} \tan^{-1} \frac{\sqrt{5V_{dd\delta} - 8V_{dd\delta'} + 4V_{dd\pi} - 16V_{dd\pi'} + 3V_{dd\sigma}}}{\sqrt{2}\sqrt{-2V_{dd\delta} + 5V_{dd\delta'} - 4V_{dd\pi} + 4V_{dd\pi'} + 3V_{dd\sigma'}}}. \quad \text{(G4)}$$

APPENDIX H: AFM DOMAIN WALL IN-GAP STATES

In this section, we analyze the in-gap states localized in the antiferromagnetic domain wall of the Sr_2IrO_4 system.

The Full Hamiltonian

The tight-binding (TB) Hamiltonian of a single-layer strontium iridate is given by

$$H(\mathbf{k}) = (\varepsilon_2(\mathbf{k},\theta) + \varepsilon_3(\mathbf{k},\theta))\sigma_0\tau_0 + \varepsilon_1(\mathbf{k},\theta)\sigma_0\tau_x + \varepsilon_{1d}(\mathbf{k},\theta)\sigma_z\tau_y, \quad \text{(H1)}$$

where

$$\varepsilon_2(\mathbf{k},\theta) = 4t_2(\theta)\cos k_x \cos k_y$$

$$\varepsilon_3(\mathbf{k},\theta) = 2t_3(\theta)(\cos 2k_x + \cos 2k_y)$$

$$\varepsilon_1(\mathbf{k},\theta) = 2t_1(\theta)(\cos k_x + \cos k_y)$$

$$\varepsilon_{1d}(\mathbf{k},\theta) = 2t_{1d}(\theta)(\cos k_x + \cos k_y).$$

Or, rewriting the above equation in matrix form, we have

$$H(k_x, k_y)$$

$$= (4t_2 \cos k_x \cos k_y + 2t_3(\cos 2k_x + \cos 2k_y))\sigma_0\tau_0$$

$$+ \begin{pmatrix} 0 & 2(t_1 - it_{1d})(\cos k_x + \cos k_y) & 0 & 0 \\ 2(t_1 + it_{1d})(\cos k_x + \cos k_y) & 0 & 0 & 0 \\ 0 & 0 & 0 & 2(t_1 + it_{1d})(\cos k_x + \cos k_y) \\ 0 & 0 & 2(t_1 - it_{1d})(\cos k_x + \cos k_y) & 0 \end{pmatrix}.$$

$$\text{(H2)}$$

When we introduce a magnetic ordering into the system, the Hamiltonian becomes

$$H(k_x, k_y)$$
$$= (4t_2 \cos k_x \cos k_y + 2t_3(\cos 2k_x + \cos 2k_y))\sigma_0\tau_0$$

$$+ \begin{pmatrix} 0 & 2(t_1 - it_{1d})(\cos k_x + \cos k_y) & m_x^A - im_y^A & 0 \\ 2(t_1 + it_{1d})(\cos k_x + \cos k_y) & 0 & 0 & m_x^B - im_y^B \\ m_x^A + im_y^A & 0 & 0 & 2(t_1 + it_{1d})(\cos k_x + \cos k_y) \\ 0 & m_x^B + im_y^B & 2(t_1 - it_{1d})(\cos k_x + \cos k_y) & 0 \end{pmatrix}.$$

(H3)

For the sake of convenience in later calculations, we choose a new set of coordinates $(K_X, K_Y) = \frac{1}{\sqrt{2}}(k_x + k_y, k_y - k_x)$. Then the Hamiltonian reads

$$H(K_X, K_Y) = (2t_2(\cos \sqrt{2}K_X + \cos \sqrt{2}K_Y) + 4t_3 \cos \sqrt{2}K_X \cos \sqrt{2}K_Y)\sigma_0\tau_0$$

$$+ \begin{pmatrix} 0 & 4(t_1 - it_{1d})\frac{\cos K_X}{\sqrt{2}}\frac{\cos K_Y}{\sqrt{2}} & m_x^A - im_y^A & 0 \\ 4(t_1 + it_{1d})\frac{\cos K_X}{\sqrt{2}}\frac{\cos K_Y}{\sqrt{2}} & 0 & 0 & m_x^B - im_y^B \\ m_x^A + im_y^A & 0 & 0 & 4(t_1 + it_{1d})\frac{\cos K_X}{\sqrt{2}}\frac{\cos K_Y}{\sqrt{2}} \\ 0 & m_x^B + im_y^B & 4(t_1 - it_{1d})\frac{\cos K_X}{\sqrt{2}}\frac{\cos K_Y}{\sqrt{2}} & 0 \end{pmatrix}.$$

(H4)

The low energy effective Hamiltonian

We already know that the band structure of the Hamiltonian (2) has a fourfold degenerate nodal line, close to the Fermi energy, along the Brillouin zone (BZ) boundary. Since we are interested in the low energy physics near the Fermi level, we expand the Hamiltonian around a certain point on the BZ boundary (K_{X0}, K_{Y0}). As we set $(K_{X0}, K_{Y0}) = (0, \pi/\sqrt{2})$,

$$H(\delta K_X, \delta K_Y) + 4t_3\sigma_0\tau_0$$
$$= \begin{pmatrix} 0 & -2\sqrt{2}(t_1 - it_{1d})\delta K_Y & m_x^A - im_y^A & 0 \\ -2\sqrt{2}(t_1 + it_{1d})\delta K_Y & 0 & 0 & m_x^B - im_y^B \\ m_x^A + im_y^A & 0 & 0 & -2\sqrt{2}(t_1 + it_{1d})\delta K_Y \\ 0 & m_x^B + im_y^B & -2\sqrt{2}(t_1 - it_{1d})\delta K_Y & 0 \end{pmatrix} + \mathcal{O}(\delta K^2).$$

(H5)

The $4t_3\sigma_0\tau_0$ term does nothing but just give a constant shift to the band structure, so we neglect it from now on. Then, up to the first order of δK_i's, the effective Hamiltonian is written as

$$H(\delta K_Y) = \begin{pmatrix} 0 & -2\sqrt{2}(t_1 - it_{1d})\delta K_Y & m_x^A - im_y^A & 0 \\ -2\sqrt{2}(t_1 + it_{1d})\delta K_Y & 0 & 0 & m_x^B - im_y^B \\ m_x^A + im_y^A & 0 & 0 & -2\sqrt{2}(t_1 + it_{1d})\delta K_Y \\ 0 & m_x^B + im_y^B & -2\sqrt{2}(t_1 - it_{1d})\delta K_Y & 0 \end{pmatrix}.$$

(H6)

A single domain

To consider a single domain with the net ferromagnetic moment in the $+Y$ direction, we put

$$m_x^A = m \cos\alpha, \quad m_y^A = m \sin\alpha$$
$$m_x^B = -m \sin\alpha, \quad m_y^B = -m \cos\alpha,$$

(H7)

where m and α are positive real constants which denote the magnitude of the magnetic ordering and the angle between the $\vec{m}^A$ and x axis, respectively. The Hamiltonian with such a configuration has several local symmetries: G, C, and M.

$$G = \frac{1}{\sqrt{2}}(\sigma_x - \sigma_y)\tau_x$$

$$C = \frac{1}{\sqrt{2}}(\sigma_x + \sigma_y)\tau_y$$

(H8)

$$M = \sigma_z\tau_z$$

$H(\delta K_Y)$ commutes with G and anticommutes with C and M. Using the following similarity transformation U that diagonalizes G [$UGU^\dagger = \text{diag}(-1, -1, 1, 1)$],

$$U = \begin{pmatrix} -\frac{1-i}{2} & 0 & 0 & \frac{1}{\sqrt{2}} \\ 0 & -\frac{1-i}{2} & \frac{1}{\sqrt{2}} & 0 \\ \frac{1-i}{2} & 0 & 0 & \frac{1}{\sqrt{2}} \\ 0 & \frac{1-i}{2} & \frac{1}{\sqrt{2}} & 0 \end{pmatrix},$$

(H9)

we can block diagonalize $H(\delta K_Y)$ into

$$H'(\delta K_Y) = UH(\delta K_Y)U^\dagger$$
$$= \begin{pmatrix} H_u(\delta K_Y) & 0 \\ 0 & H_l(\delta K_Y) \end{pmatrix},$$

(H10)

where

$$H_u(\delta K_Y) = \begin{pmatrix} 0 & -\tilde{t}\delta K_Y - \tilde{m} \\ -\tilde{t}^*\delta K_Y - \tilde{m}^* & 0 \end{pmatrix},$$

$$H_l(\delta K_Y) = \begin{pmatrix} 0 & -\tilde{t}\delta K_Y + \tilde{m} \\ -\tilde{t}^*\delta K_Y + \tilde{m}^* & 0 \end{pmatrix}. \quad \text{(H11)}$$

Here, $\tilde{t}$ and $\tilde{m}$ are defined as $\tilde{t} = 2\sqrt{2}(t_3 - it_4)$ and $\tilde{m} = me^{-i(\alpha + \frac{\pi}{4})}$.

Eigenvalues of each blocks are given by

$$E_u(\delta K_Y) = \pm|\tilde{t}\delta K_Y + \tilde{m}|,$$

$$E_l(\delta K_Y) = \pm|\tilde{t}\delta K_Y - \tilde{m}|. \quad \text{(H12)}$$

When δK_Y goes to zero, the eigenvalues become $\pm m$. Thus, we confirm that a gap with size $2m$ opens at the point $(K_{X0}, K_{Y0}) = (0, \pi/\sqrt{2})$ in the case of the single magnetic domain.

A domain wall along the [110] direction

Now we think about a system with a domain wall that separates two domains with different net ferromagnetic moments: one in the $+Y$ direction, and the other in the $-Y$ direction. We can get the Hamiltonian of such a system by modifying the magnetic ordering used in the previous section. In this section, we investigate three different types of domain wall models: smooth, Néel, and Bloch domain wall.

a. Smooth wall

First, we consider the simplest model, in which the magnitude of the magnetic moments changes, but their directions stay still. In such a *smooth wall*, the magnitude of the magnetic moments is smoothly scaled down to zero in the transition region. Multiplying $\tanh(\beta Y)$ to Eq. (H7), we have the smooth wall configuration with the domain wall lying in the $Y = 0$ plane.

$$m_x^A = m\cos\alpha\tanh(\beta Y),$$

$$m_y^A = m\sin\alpha\tanh(\beta Y),$$

$$m_x^B = -m\sin\alpha\tanh(\beta Y),$$

$$m_y^B = -m\cos\alpha\tanh(\beta Y). \quad \text{(H13)}$$
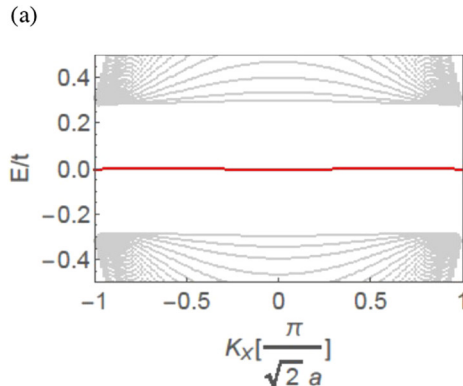
The role of $\tanh(\beta Y)$ here is to invert the magnetic moments as Y changes its sign, where $|\beta|$ determines the stiffness of the domain wall profile.

Under the similar transformation introduced in the previous section of the single domain wall (Appendix H 3), M transforms into $M' = \sigma_0\tau_z$. As H anticommutes with M, H' anticommutes with M'. Thus, both of the 2×2 block Hamiltonians anticommute with τ_z. Because H_u and H_l anticommute with τ_z, if these block Hamiltonians have zero energy eigenstates, the zero eigenstates should also be eigenstates of τ_z, so they are of the form $\binom{f(Y)}{0}$ or $\binom{0}{g(Y)}$. In the presence of the domain wall, the periodicity of the system along the Y direction is broken, and thus K_Y is no more a good quantum number. Therefore, we replace δK_Y by $(-i\partial_Y)$ to solve the Hamiltonian equation. Then we have

$$H_{u,\text{scale}}(\partial_Y) = \begin{pmatrix} 0 & i\tilde{t}\partial_Y - \tilde{m}\tanh(\beta Y) \\ i\tilde{t}^*\partial_Y - \tilde{m}^*\tanh(\beta Y) & 0 \end{pmatrix},$$

$$H_{l,\text{scale}}(\partial_Y) = \begin{pmatrix} 0 & i\tilde{t}\partial_Y + \tilde{m}\tanh(\beta Y) \\ i\tilde{t}^*\partial_Y + \tilde{m}^*\tanh(\beta Y) & 0 \end{pmatrix}. \quad \text{(H14)}$$

For the upper block, $(i\tilde{t}^*\partial_Y - \tilde{m}^*\tanh(\beta Y))f_u(Y) = 0$ gives a solution $f_u(Y) \sim \cosh(\beta Y)^{-i\tilde{m}^*/\beta\tilde{t}^*}$, while $(i\tilde{t}\partial_Y - \tilde{m}\tanh(\beta Y))g_u(Y) = 0$ gives a solution $g_u(Y) \sim \cosh(\beta Y)^{-i\tilde{m}/\beta\tilde{t}}$. On the other hand, for the lower block, $(i\tilde{t}^*\partial_Y + \tilde{m}^*\tanh(\beta Y))f_l(Y) = 0$ gives a solution $f_l(Y) \sim \cosh(\beta Y)^{i\tilde{m}^*/\beta\tilde{t}^*}$, and $(i\tilde{t}\partial_Y + \tilde{m}\tanh(\beta Y))g_l(Y) = 0$ gives a solution $g_l(Y) \sim \cosh(\beta Y)^{i\tilde{m}/\beta\tilde{t}}$. Substituting $\tilde{m}/\tilde{t}$ to c, we can simply write the solutions in the following form

$$f_u(Y) \sim \cosh(\beta Y)^{-ic^*/\beta},$$

$$g_u(Y) \sim \cosh(\beta Y)^{-ic/\beta},$$

$$f_l(Y) \sim \cosh(\beta Y)^{ic^*/\beta},$$

$$g_l(Y) \sim \cosh(\beta Y)^{ic/\beta}. \quad \text{(H15)}$$

In general, only two of these solutions are physically allowed, since we must discard solutions whose norms diverge as $Y \to \pm\infty$. Which solutions survive depends on the signs of m, α,
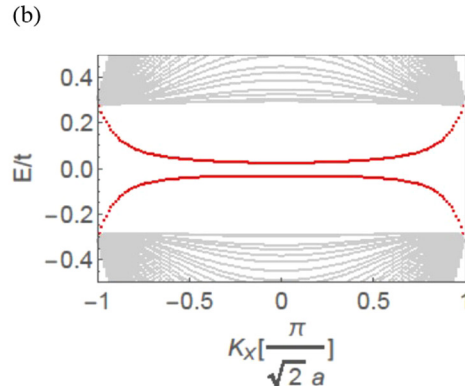
(a)

(b)

FIG. 12. Dispersion of domain wall states of the smooth wall (a) with and (b) without zero magnetic moment atoms at the domain wall position.
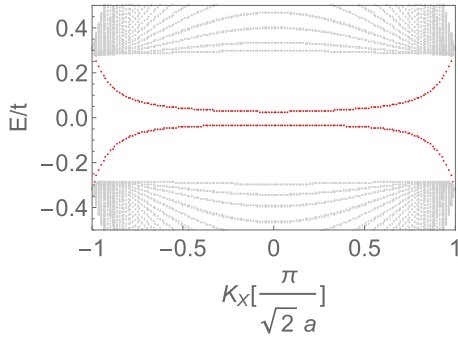
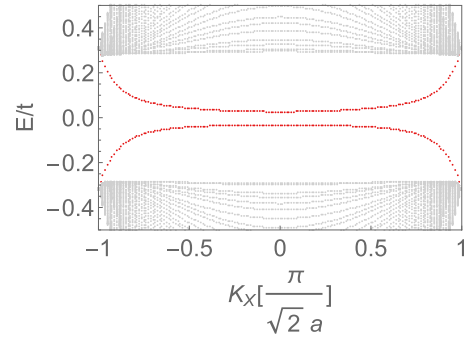FIG. 13. Dispersion of domain wall states of the Néel wall.

FIG. 14. Dispersion of domain wall states of the Bloch wall.

and β (and on the magnitude of α as well).

$$
\begin{aligned}
c = \frac{\tilde{m}}{\tilde{t}} &= \frac{m e^{-i(\alpha + \frac{\pi}{4})}}{t_3 - i t_4} \\
&= \frac{m e^{-i(\alpha + \frac{\pi}{4})}}{|\tilde{t}| e^{-i\phi}} \\
&= \frac{m}{|\tilde{t}|} e^{-i(\alpha + \frac{\pi}{4} - \phi)},
\end{aligned} \tag{H16}
$$

where $\phi = \tan^{-1}(t_4/t_3)$, $|f_u(Y)|^2 = f_u^*(Y) f_u(Y)$ becomes

$$
\begin{aligned}
|f_u(Y)|^2 &\sim \cosh(\beta Y)^{-i \frac{m}{\beta |\tilde{t}|} (e^{i(\alpha + \frac{\pi}{4} - \phi)} - e^{-i(\alpha + \frac{\pi}{4} - \phi)})} \\
&\sim \cosh(\beta Y)^{\frac{2m}{\beta |\tilde{t}|} \sin(\alpha + \frac{\pi}{4} - \phi)}.
\end{aligned} \tag{H17}
$$

Repeating the same calculation for the other solutions, we are left with

$$
\begin{aligned}
|f_u(Y)|^2 &\sim \cosh(\beta Y)^{\frac{2m}{\beta |\tilde{t}|} \sin(\alpha + \frac{\pi}{4} - \phi)}, \\
|g_u(Y)|^2 &\sim \cosh(\beta Y)^{-\frac{2m}{\beta |\tilde{t}|} \sin(\alpha + \frac{\pi}{4} - \phi)}, \\
|f_l(Y)|^2 &\sim \cosh(\beta Y)^{-\frac{2m}{\beta |\tilde{t}|} \sin(\alpha + \frac{\pi}{4} - \phi)}, \\
|g_l(Y)|^2 &\sim \cosh(\beta Y)^{\frac{2m}{\beta |\tilde{t}|} \sin(\alpha + \frac{\pi}{4} - \phi)}.
\end{aligned} \tag{H18}
$$

Equation (H18) states that if $\frac{2m}{\beta |\tilde{t}|} < 0$, the two valid solutions would be f_u and g_l, while if $\frac{2m}{\beta |\tilde{t}|} < 0$ the valid solutions would be g_u and f_l. For example, when m and β are given to be positive, and $(\phi - \alpha) < \pi/4$, $|f_u(Y)|^2$ and $|g_l(Y)|^2$ have positive exponents, they are unphysical. Meanwhile, $|g_u(Y)|^2$ and $|f_l(Y)|^2$ have negative exponents, therefore g_u and f_l are the final solutions that we have been seeking.

However, numerical calculation for a finite size system does not always give the zero energy eigenstates. Only when the system has atoms located exactly on the domain wall thus there is a line of atoms with zero magnetic moment on the $Y = 0$ plane, i.e., $n_{DW} = 0$, the doubly degenerate zero mode appears, and otherwise, the domain wall states are gapped (See Fig. 12). It is similar to a situation that happens in the case of the Su-Schrieffer-Heeger (SSH) model; a domain wall in the SSH model exhibits zero modes if there is an atomic site right on the domain wall but does not if a bond is located on the domain wall instead of an atomic site.

b. Néel wall

When magnetic moments rotate around an axis parallel to a domain wall plane in the transition region, it is called a Néel wall. The domain wall configuration for the Néel wall is defined by

$$
\begin{aligned}
\vec{m}^A &= m(\cos\alpha \tanh(\beta Y) + \sin\alpha \operatorname{sech}(\beta Y), -\cos\alpha \operatorname{sech}(\beta Y) + \sin\alpha \tanh(\beta Y), 0), \\
\vec{m}^B &= -m(\sin\alpha \tanh(\beta Y) + \cos\alpha \operatorname{sech}(\beta Y), -\sin\alpha \operatorname{sech}(\beta Y) + \cos\alpha \tanh(\beta Y), 0).
\end{aligned} \tag{H19}
$$

Then the transformed effective Hamiltonian becomes

$$
H'_{\text{Neel}}(\delta K_Y) = \begin{pmatrix} 0 & -\tilde{t}\delta K_Y - \tilde{m}\tanh(\beta Y) & 0 & -i\tilde{m}\operatorname{sech}(\beta Y) \\ -\tilde{t}^*\delta K_Y - \tilde{m}^*\tanh(\beta Y) & 0 & -i\tilde{m}^*\operatorname{sech}(\beta Y) & 0 \\ 0 & i\tilde{m}\operatorname{sech}(\beta Y) & 0 & -\tilde{t}\delta K_Y + \tilde{m}\tanh(\beta Y) \\ i\tilde{m}^*\operatorname{sech}(\beta Y) & 0 & -\tilde{t}^*\delta K_Y + \tilde{m}^*\tanh(\beta Y) & 0 \end{pmatrix}. \tag{H20}
$$

Unlike $H_{u,\text{scale}}$ and $H_{l,\text{scale}}$ which were totally decoupled, it is obvious that $H_{u,\text{Neel}}$ and $H_{l,\text{Neel}}$ are coupled to each other. It means that the two domain wall states are mixed and a gap opens (See Fig. 13).

c. Bloch wall

When magnetic moments rotate around an axis perpendicular to the domain wall plane in the transition region, it is called a Bloch wall. The domain wall configuration for the Bloch wall is defined by

$$\vec{m}^A = m(\cos\alpha\tanh(\beta Y), \sin\alpha\tanh(\beta Y), \text{sech}(\beta Y)),$$

$$\vec{m}^B = -m(\sin\alpha\tanh(\beta Y), \cos\alpha\tanh(\beta Y), \text{sech}(\beta Y)). \tag{H21}$$

Then the transformed effective Hamiltonian becomes

$$H'_{\text{Bloch}}(\delta K_Y) = \begin{pmatrix} m\,\text{sech}(\beta Y) & -\tilde{t}\delta K_Y - \tilde{m}\tanh(\beta Y) & 0 & 0 \\ -\tilde{t}^*\delta K_Y - \tilde{m}^*\tanh(\beta Y) & -m\,\text{sech}(\beta Y) & 0 & 0 \\ 0 & 0 & m\,\text{sech}(\beta Y) & -\tilde{t}\delta K_Y + \tilde{m}\tanh(\beta Y) \\ 0 & 0 & -\tilde{t}^*\delta K_Y + \tilde{m}^*\tanh(\beta Y) & -m\,\text{sech}(\beta Y) \end{pmatrix}. \tag{H22}$$

This time, $H'_{u/l,\text{Bloch}}$ no more anticommutes with τ_z, so the zero modes do not exist (See Fig. 14).

---

[1] R. E. Peierls, *Quantum theory of solids*, Vol. 23 (Oxford University Press, London, 1955).

[2] R. Shankar, Renormalization-group approach to interacting fermions, Rev. Mod. Phys. **66**, 129 (1994).

[3] C. J. Bradley, and A. P. Cracknell, *The Mathematical Theory of Symmetry in Solids* (Clarendon Press, Oxford, 1972).

[4] B. J. Wieder, and C. L. Kane, Spin-orbit semimetals in the layer groups, Phys. Rev. B **94**, 155108 (2016).

[5] S. M. Young, and C. L. Kane, Dirac Semimetals in Two Dimensions, Phys. Rev. Lett. **115**, 126803 (2015).

[6] M. Braden, G. Andre, S. Nakatsuji, and Y. Maeno, Crystal and magnetic structure of Ca_2RuO_4: Magnetoelastic coupling and the metal-insulator transition, Phys. Rev. B **58**, 847 (1998).

[7] J.-M. Carter, V. Shankar V., and H.-Y. Kee, Theory of metal-insulator transition in the family of perovskite iridium oxides, Phys. Rev. B **88**, 035111 (2013).

[8] M. A. Subramanian, M. K. Crawford, R. L. Harlow, T. Ami, J. A. Fernandez-Baca, Z. R. Wang, and D. C. Johnston, Sr_2RhO_4 and Sr_2IrO_4: Structural and magnetic studies of $4d$ and $5d$ transition metal analogs of La_2CuO_4, Physica C: Superconductivity **235**, 743 (1994).

[9] F. Ye, X. Wang, C. Hoffmann, J. Wang, S. Chi, M. Matsuda, B. C. Chakoumakos, J. A. Fernandez-Baca, and G. Cao, Structure symmetry determination and magnetic evolution in $Sr_2Ir_{1-x}Rh_xO_4$, Phys. Rev. B **92**, 201112(R) (2015).

[10] M. K. Crawford, M. A. Subramanian, R. L. Harlow, J. A. Fernandez-Baca, Z. R. Wang, and D. C. Johnston, Structural and magnetic studies of Sr_2IrO_4, Phys. Rev. B **49**, 9198 (1994).

[11] S. J. Yuan, S. Aswartham, J. Terzic, H. Zheng, H. D. Zhao, P. Schlottmann, and G. Cao, From $J_{\text{eff}} = 1/2$ insulator to p-wave superconductor in single-crystal $Sr_2Ir_{1-x}Ru_xO_4 (0 \leqslant x \leqslant 1)$, Phys. Rev. B **92**, 245103 (2015).

[12] J. M. Rondinelli, and N. A. Spaldin, Structure and Properties of Functional Oxide Thin Films: Insights From Electronic-Structure Calculations, Adv. Mater. **23**, 3363 (2011).

[13] J. D. Axe, A. H. Moudden, D. Hohlwein, D. E. Cox, K. M. Mohanty, A. R. Moodenbaugh, and Y. Xu, Structural Phase Transformations and Superconductivity in $La_{2-x}Ba_xCuO_4$, Phys. Rev. Lett. **62**, 2751 (1989).

[14] E. S. Bozin, R. Zhong, K. R. Knox, G. Gu, J. P. Hill, J. M. Tranquada, and S. J. L. Billinge, Reconciliation of local and long-range tilt correlations in underdoped $La_{2-x}Ba_xCuO_4 (0 \leqslant x \leqslant 0.155)$, Phys. Rev. B **91**, 054521 (2015).

[15] B.-J. Yang, and N. Nagaosa, Classification of stable three-dimensional Dirac semimetal with nontrivial topology, Nat. Commun. **5**, 4898 (2014).

[16] B.-J. Yang, T. A. Bojesen, T. Morimoto, and A. Furusaki, Topological semimetals protected by off-centered symmetries in nonsymmorphic crystals, Phys. Rev. B **95**, 075135 (2017).

[17] B. J. Kim, H. Ohsumi, T. Komesu, S. Sakai, T. Morita, H. Takagi, and T. Arima, Phase-Sensitive Observation of a Spin-Orbital Mott State in Sr_2IrO_4, Science **323**, 1329 (2009).

[18] S. J. Moon, H. Jin, K. W. Kim, W. S. Choi, Y. S. Lee, J. Yu, G. Cao, A. Sumi, H. Funakubo, C. Bernhard, and T. W. Noh, Dimensionality-Controlled Insulator-Metal Transition and Correlated Metallic State in $5d$ Transition Metal Oxides $Sr_{n+1}Ir_nO_{3n+1}$ ($n = 1, 2$, and ∞), Phys. Rev. Lett. **101**, 226402 (2008).

[19] B. J. Kim, H. Jin, S. J. Moon, J.-Y. Kim, B.-G. Park, C. S. Leem, J. Yu, T. W. Noh, C. Kim, S.-J. Oh, J.-H. Park, V. Durairaj, G. Cao, and E. Rotenberg, Novel $J_{\text{eff}} = 1/2$ Mott State Induced by Relativistic Spin-Orbit Coupling in Sr_2IrO_4, Phys. Rev. Lett. **101**, 076402 (2008).

[20] H. Jin, H. Jeong, T. Ozaki, and J. Yu, Anisotropic exchange interactions of spin-orbit-integrated states in Sr_2IrO_4, Phys. Rev. B **80**, 075112 (2009).

[21] G. Jackeli, and G. Khaliullin, Mott Insulators in the Strong Spin-Orbit Coupling Limit: From Heisenberg to a Quantum Compass and Kitaev Models, Phys. Rev. Lett. **102**, 017205 (2009).

[22] F. Wang, and T. Senthil, Twisted Hubbard Model for Sr_2IrO_4: Magnetism and Possible High Temperature Superconductivity, Phys. Rev. Lett. **106**, 136402 (2011).

[23] J. C. Slater, and G. F. Koster, Simplified LCAO Method for the Periodic Potential Problem, Phys. Rev. **94**, 1498 (1954).

[24] D. L. Bergman, C. Wu, and L. Balents, Band touching from real-space topology in frustrated hopping models, Phys. Rev. B **78**, 125104 (2008).

[25] J. Kim, D. Casa, M. H. Upton, T. Gog, Y.-J. Kim, J. F. Mitchell, M. van Veenendaal, M. Daghofer, J. van den Brink, G. Khaliullin, and B. J. Kim, Magnetic Excitation Spectra of Sr_2IrO_4 Probed by Resonant Inelastic X-Ray

Scattering:Establishing Links to Cuprate Superconductors, Phys. Rev. Lett. **108**, 177003 (2012).

[26] H. Okabe, M. Isobe, E. Takayama-Muromachi, A. Koda, S. Takeshita, M. Hiraishi, M. Miyazaki, R. Kadono, Y. Miyake, and J. Akimitsu, Ba_2IrO_4: A spin-orbit Mott insulating quasi-two-dimensional antiferromagnet, Phys. Rev. B **83**, 155118 (2011).

[27] W. P. Su, J. R. Schrieffer, and A. J. Heeger, Soliton excitations in polyacetylene, Phys. Rev. B **22**, 2099 (1980).

[28] E. Y. Ma, Y.-T. Cui, K. Ueda, S. Tang, K. Chen, N. Tamura, P. M. Wu, J. Fujioka, Y. Tokura, and Z.-X. Shen, Mobile metallic domain walls in an all-in-all-out magnetic insulator, Science **350**, 538 (2015).

[29] F.-T. Huang, and S.-W. Cheong, Aperiodic topological order in the domain configurations of functional materials, Nature Reviews Materials **2**, 17004 (2017).

[30] A. de la Torre, S. McKeown Walker, F. Y. Bruno, S. Riccó, Z. Wang, I. Gutierrez Lezama, G. Scheerer, G. Giriat, D. Jaccard, C. Berthod, T. K. Kim, M. Hoesch, E. C. Hunter, R. S. Perry, A. Tamai, and F. Baumberger, Collapse of the Mott Gap and Emergence of a Nodal Liquid in Lightly Doped Sr_2IrO_4, Phys. Rev. Lett. **115**, 176402 (2015).

[31] S. Zhou, K. Jiang, H. Chen, and Z. Wang, Correlation effects and hidden spin-orbit entangled electronic order in parents and electron-doped iridates Sr_2IrO_4, Phys. Rev. X **7**, 041018 (2017).

[32] P. Liu, M. Reticcioli, B. Kim, A. Continenza, G. Kresse, D. D. Sarma, X.-Q. Chen, and C. Franchini, Electron and hole doping in the relativistic Mott insulator Sr_2IrO_4: a first principles study using band unfolding technique, Phys. Rev. B **94**, 195145 (2016).

[33] B. J. Kim, J. Yu, H. Koh, I. Nagai, S. I. Ikeda, S.-J. Oh, and C. Kim, Missing *xy*-band Fermi Surface in 4*d* Transition-Metal Oxide Sr_2RhO_4: Effect of the Octahedra Rotation on the Electronic Structure, Phys. Rev. Lett. **97**, 106401 (2006).

[34] G.-Q. Liu, V. N. Antonov, O. Jepsen, and O. K. Andersen, Coulomb-Enhanced Spin-Orbit Splitting: the Missing Piece in the Sr_2RhO_4 Puzzle, Phys. Rev. Lett. **101**, 026408 (2008).

[35] K.-H. Ahn, K.-W. Lee, and J. Kunes, Doping-dependent bandwidth renormalization and spin-orbit coupling in $(Sr_{1-x}La_x)_2RhO_4$, J. Phys: Condens. Matter **27**, 085602 (2015).

[36] F. Ye, S. Chi, B. C. Chakoumakos, J. A. Fernandez-Baca, T. Qi, and G. Cao, Magnetic and crystal structures of Sr_2IrO_4 : A neutron diffraction study, Phys. Rev. B **87**, 140406(R) (2013).

[37] D. H. Torchinsky, H. Chu, L. Zhao, N. B. Perkins, Y. Sizyuk, T. Qi, G. Cao, and D. Hsieh, Structural Distortion-Induced Magnetoelastic Locking in Sr_2IrO_4 Revealed through Nonlinear Optical Harmonic Generation, Phys. Rev. Lett. **114**, 096404 (2015).

[38] R. Arita, J. Kunes, P. Augustinsky, A. V. Kozhevnikov, A. G. Eguiluz, and M. Imada, Mott versus Slater-type metal-insulator transition in Sr_2IrO_4 and Ba_2IrO_4, JPS Conf. Proc. **3**, 013023 (2014).

[39] http://elk.sourceforge.net.

[40] J. P. Perdew, and Y. Wang, Accurate and simple analytic representation of the electron-gas correlation energy, Phys. Rev. B **45**, 13244 (1992).

[41] J. Rath, and A. J. Freeman, Generalized magnetic susceptibilities in metals: Application of the analytic tetrahedron linear energy method to Sc, Phys. Rev. B **11**, 2109 (1975).